1   # Specification of axial identity by Hoxa2 distinguishes between a

2   # phenotypic and molecular ground state in mouse cranial neural crest cells

3

4   Irina Pushel[1], Paul A Trainor[1,2], Robb Krumlauf[1,2]*

5   1. Stowers Institute for Medical Research, Kansas City, MO 64110, USA

6   2. Department of Anatomy and Cell Biology, University of Kansas Medical Center, Kansas

7   City, KS 66160, USA

8   *corresponding author, rek@stowers.org

9

10   **Abstract**

11   *Hox* genes play a key role in head formation by specifying the axial identity of neural

12   crest cells (NCCs) migrating into embryonic pharyngeal arches. In the absence of *Hoxa2*, NCC

13   derivatives of the second pharyngeal arch (PA2) undergo a homeotic transformation and

14   duplicate structures formed by first arch (PA1) NCCs. Current models postulate that PA1

15   represents a NCC 'ground state' and loss of *Hoxa2* causes a reversion of PA2 NCCs to the PA1

16   'ground state'. We use bulk and single-cell RNAseq to investigate the molecular mechanisms

17   driving this phenotypic transformation in the mouse. In *Hoxa2*^{-/-} mutants, PA2 NCCs generally

18   maintain expression of the PA2 transcriptional signature and fail to strongly upregulate a PA1

19   transcriptional signature. Our analyses identify putative HOXA2 targets and suggest that

20   subsets of NCCs may respond to HOXA2 activity in distinct manners. This separation of

21   phenotypic and molecular states has significant implications for understanding craniofacial

22   development.

Introduction

Neural crest cells (NCCs) represent one of the defining traits in the evolution of vertebrates (Sauka-Spengler et al. 2007; Green et al. 2015). The neural crest is a transient population of cells that arises along the anterior-posterior axis of the developing central nervous system (Knecht and Bronner-Fraser 2002). NCCs delaminate from the neural epithelium and migrate into the periphery of vertebrate embryos. These migratory and proliferative cells are multipotent and play a dynamic role in vertebrate development, giving rise to diverse structures including neurons, glia, pigment cells, and craniofacial bone and cartilage (LaBonne and Bronner-Fraser 1998; Le Douarin and Kalcheim 1999; Minoux and Rijli 2010). They are divided into trunk and cranial NCCs: trunk NCCs primarily contribute to the peripheral nervous system, while cranial NCCs also give rise to most of the bone and connective tissue of the head and play a key role in craniofacial morphogenesis.

The establishment of cranial NCCs is thought to have been an important step in evolution of the vertebrate head (Northcutt and Gans 1983; Parker et al. 2016; Square et al. 2017). Mutations in genes important for cranial NCC development have been shown to play a role in human craniofacial defects and disorders, making a deeper understanding of NCC development a relevant area of clinical study (Crane and Trainor 2006; Terrazas et al. 2017; Etchevers et al. 2019). Cranial NCCs are initially specified at the neural plate border region, together with neural precursors (LaBonne and Bronner-Fraser 1999; Le Douarin and Kalcheim 1999; Knecht and Bronner-Fraser 2002). The NCCs then delaminate from the dorsal neural tube and migrate into the frontonasal prominence and pharyngeal arches (PAs), highly conserved transient embryonic structures that form the oral apparatus which is essential for feeding and breathing. Upon arrival at their destination, NCCs differentiate into the derivative structures that shape the vertebrate head (Couly et al. 1993)(Fig. 1A,B). NCCs give rise to unique structures based on their axial level of origin (Kontges and Lumsden 1996). For instance, the NCCs migrating into the first PA (PA1) contribute to the maxillary and mandibular components of the jaw, Meckel's cartilage, and the incus and malleus of the middle ear, while the NCCs migrating into the second PA (PA2) form the stapes of the middle ear and the hyoid bone in the neck (Le Douarin and Kalcheim 1999; Minoux and Rijli 2010).

2

52
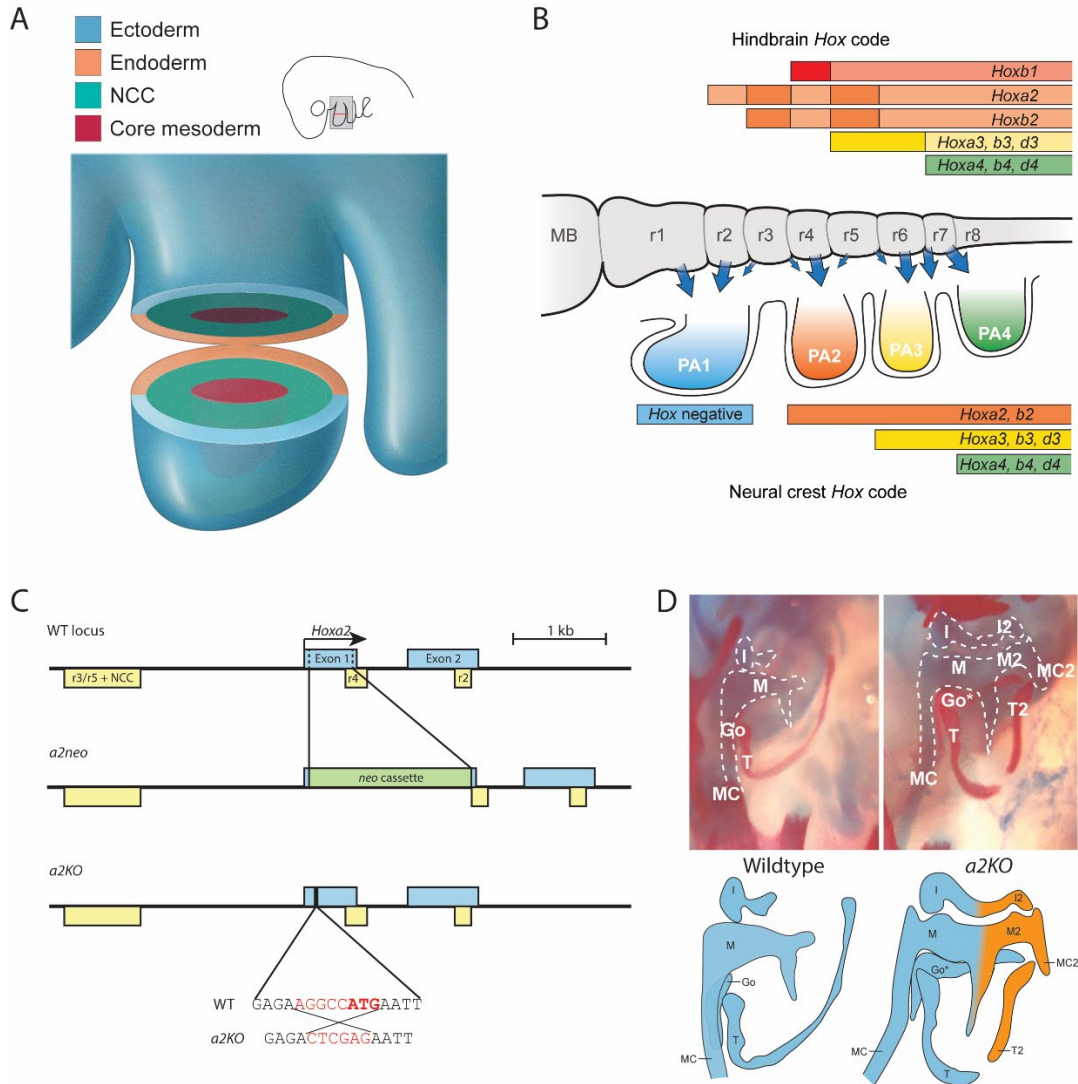
Figure 1. *Hox* genes in the PAs and phenotypic effects of *Hoxa2* knockout. A) NCCs migrate into the PAs surrounding a mesodermal core, contained within the ectoderm and endoderm surrounding the PA structure. Schematic corresponds to ~E9.0-E9.5 mouse embryo. B) *Hox* genes are expressed in a nested pattern that affects NCC fate prior to delamination and migration (hindbrain code, top) and a distinct pattern once the cells have populated the PAs (neural crest code, bottom). Figure adapted from (Parker et al. 2018). C) A comparison of the WT *Hoxa2* locus to the *a2neo* and *a2KO* alleles. Exons depicted in blue, enhancers in yellow. Bottom depicts 7-bp change (highlighted in red) between WT and *a2KO* alleles. Start codon (ATG) bold. D) Comparison of middle ear skeletal staining at E18.5 between embryos that are WT and homozygous for the *a2KO* allele. Cartilagenous structures outlined with white dashed line for clarity. Schematics show PA1-derived structures in blue and PA2-derived structures in orange. M=malleus, I=incus, MC=Meckel's cartilage, T=Tympanic bone, Go=gonial bone. Duplicated structures designated with a 2 (M2, I2, MC2, T2); Go*=transformed gonial bone.

3

66   The highly conserved family of HOX transcription factors plays a key role in establishing

67   regional identities in diverse tissues throughout animal development (Carroll 1995; Alexander

68   et al. 2009; Mallo et al. 2010). During vertebrate head development, the expression and

69   function of *Hox* genes are tightly coupled with the specification of axial identity in hindbrain

70   segments and cranial NCCs (Hunt et al. 1991; Couly et al. 1998; Trainor and Krumlauf 2000b;

71   Trainor and Krumlauf 2001; Minoux and Rijli 2010; Parker et al. 2018). In the developing mouse

72   embryo, NCCs express *Hox* genes in two general phases during their development: prior to their

73   delamination from the neural tube (the 'hindbrain *Hox* code') and after they begin migrating

74   into the PAs (the 'neural crest *Hox* code') (Fig 1B). This establishes a colinear nested expression

75   pattern of *Hox* genes in the PAs: PA1 NCCs lack *Hox* expression, PA2 NCCs express *Hoxa2* and

76   *Hoxb2*, PA3 NCCs express *Hoxa2*, *Hoxb2*, *Hoxa3*, *Hoxb3*, and *Hoxd3*, and so on into more

77   posterior arches (Hunt et al. 1991; Minoux and Rijli 2010; Parker et al. 2018). This generates a

78   combinatorial *Hox* code that underlies the establishment of unique axial identities of each PA

79   (Trainor and Krumlauf 2001).

80   Whether *Hox* codes are first established in the hindbrain and transferred into the

81   periphery by migrating NCCs or initiated independently in NCCs separate from the hindbrain

82   *Hox* code is not well understood. Regulatory studies have generated evidence for both

83   independent and shared regulation of *Hoxa2* and *Hoxb2* genes in hindbrain segments and

84   cranial NCCs (Maconochie et al. 1997; Maconochie et al. 1999; McEllin et al. 2016; Parker et al.

85   2019). Heterotopic grafting experiments in zebrafish and mouse embryos have revealed that

86   *Hox* expression in NCCs is not permanently fixed and is influenced by signals from the PA

87   environment (Trainor and Krumlauf 2000a; Trainor and Krumlauf 2000b; Schilling et al. 2001).

88   This suggests there is dynamic regulation of *Hox* expression during NCC formation and

89   migration in the PAs. However, it remains unclear whether the NCC *Hox* code acts in parallel to

90   or directly within the emerging framework for the conserved core gene regulatory network

91   governing NCC development (Gammill and Bronner-Fraser 2002; Simoes-Costa and Bronner

92   2015; Martik and Bronner 2017; Parker et al. 2018; Martik et al. 2019).

93   Loss and gain of function experiments of the *Hox* genes in a number of vertebrate

94   species have led to the formulation of a NCC ground state model for axial patterning of the PAs

4

95   during embryonic development. In this model, NCCs migrating into the PAs share a common

96   default patterning program, or ground state, that is modified by combinations of *Hox* gene

97   expression to produce distinct derivatives at each axial level (Couly et al. 1998; Minoux and Rijli

98   2010; Vieux-Rochas et al. 2013). Since NCCs in PA1 lack *Hox* expression, they are postulated to

99   represent the ground state. This hypothesis is largely based on phenotypes associated with

100   perturbation of *Hoxa2* expression. In mouse *Hoxa2*$^{-/-}$ mutants, PA2-derived skeletal structures

101   display homeotic transformations and duplicate PA1-derived structures (Gendron-Maguire et

102   al. 1993; Rijli et al. 1993). Conversely, ectopic expression of *Hoxa2* in PA1 NCCs results in

103   transformation of PA1-derived skeletal structures to duplicate PA2 derivatives (Kitazawa et al.

104   2015). This functional role for *Hoxa2* in patterning PA identity has also been observed in other

105   vertebrate species (Grammatopoulos et al. 2000; Pasqualetti et al. 2000; Hunter and Prince

106   2002). Together, this evidence supports a conserved role for *Hoxa2* as a master regulator or

107   selector gene that modifies the *Hox*-free NCC ground state to impart a PA2 identity on the NCCs

108   colonizing PA2. However, the precise timing of this *Hoxa2*-dependent process remains

109   unknown, as do the cell populations and downstream target genes through which *Hoxa2* acts to

110   regulate regional identity. There is evidence of a continued requirement for *Hoxa2* activity in

111   NCCs during differentiation (Santagati et al. 2005), but an earlier role for its input into

112   programming the cranial NCCs remains unclear.

113   In addition to the specific perturbation of *Hoxa2* expression, deletion of the entire *HoxA*

114   cluster in the mouse results in PAs 2-4 all producing additional PA1-like structures in lieu of

115   caudal derivatives. This further supports the existence of a *Hox*-free ground state that is

116   transformed in each of the PAs by distinct combinations of *Hox* gene expression (Minoux et al.

117   2009). It is clear from the phenotypic transformations observed in mutant embryos that there

118   exists a phenotypic NCC ground state represented by the set of NCC derivatives produced in the

119   absence of *Hox* gene expression. Whether this phenotypic ground state is accompanied by a

120   shared molecular ground state – a transcriptional signature – that corresponds to *Hox*-free

121   NCCs and is observed in *Hox* mutant embryos, has not yet been addressed. Where the term

122   'ground state' has been used to date, the explicit distinction between a phenotypic and

123   molecular ground state has not been made (Rijli et al. 1993; Minoux et al. 2009; Amin et al.

124   2015). This is an important issue to resolve for understanding regulatory mechanisms that

125   pattern craniofacial development, because *Hoxa2* could be working to modify the properties of

126   all NCCs in PA2 or only sub-populations of cells required for specifying PA2 derived structures.

127   Regardless of the process, *Hoxa2* clearly has a fundamental effect in determining PA2 identity.

128   Recent advances in sequencing technologies enable us to more thoroughly explore the

129   molecular underpinnings of axial specification and distinguish between phenotypic and

130   transcriptional effects at single-cell resolution. Several studies have provided comparative

131   analysis of gene expression in the PAs (Brunskill et al. 2014; Lumb et al. 2017; Minoux et al.

132   2017). However, these comparisons have not yet been extended to *Hox* mutant embryos, and

133   thus lack the power to determine whether a *Hox*-free mutant PA (other than PA1) reverts not

134   only at the phenotypic level but also at the molecular or transcriptional level to a PA1-like state.

135   Thus, elucidating the molecular mechanism by which *Hoxa2* expression acts to impart a PA2

136   NCC fate directly informs our understanding of the transcriptional basis of axial identity

137   specification in the developing mouse embryo.

138   In this study, to deepen our understanding of the role of *Hoxa2* in regulating PA2

139   identity, we have used bulk and single cell RNAseq in mice, comparing wildtype (WT) and *Hoxa2*

140   mutant embryos, to investigate the precise timing and populations of cells where it exerts its

141   regulatory activity on NCCs. Strikingly, our data do not show a global reversion of the *Hoxa2*$^{-/-}$

142   PA2 transcriptional profile in NCCs to a PA1-like state, as would be expected in the presence of

143   a molecular NCC ground state. Rather, we find evidence that *Hoxa2* exerts its regulatory activity

144   in distinct subpopulations of cells in PA2 as NCCs are undergoing differentiation. Using

145   differential expression analyses from transcriptional profiling of cell populations and single

146   cells, we identified both previously described and novel putative targets of *Hoxa2* involved in

147   PA2 fate specification. Taken together, our data suggest that the phenotypic ground state of

148   mouse cranial NCCs is not matched with an underlying molecular ground state and reveal novel

149   downstream targets of *Hoxa2* involved in axial identity specification. Our findings highlight the

150   value of scRNA-seq in evaluating and refining models surrounding the molecular basis of

151   developmental and evolutionary phenotypes. Moreover, the rich transcriptomic datasets

6

152   generated in this study are a valuable resource to further characterize the molecular

153   underpinnings of NCC axial identity.

154

155

156 **Results**

157 Generation of a new mouse *Hoxa2* null allele

158   In order to investigate the molecular mechanisms by which *Hoxa2* expression drives PA2

159 fate, we used a strategy based on transcriptional profiling approaches to compare wildtype

160 (WT) and *Hoxa2* mutant mouse embryos. Existing mouse lines have mutations with a *neomycin*

161 cassette inserted into *Hoxa2* (Gendron-Maguire et al. 1993; Rijli et al. 1993), which may alter

162 the expression of neighboring *Ho*x genes, as we know this is a region rich in regulatory

163 elements both within and flanking the gene (Tümpel et al. 2006) (Fig. 1C). These lines also exist

164 on a mixed genetic background and we wanted to minimize noise in genomic comparisons by

165 performing analyses in a consistent background. In addition, we wanted to be able to monitor

166 endogenous *Hoxa2* mRNA expression in cells lacking functional HOXA2 protein. To do this, we

167 generated a novel null allele by using CRISPR-Cas9 gene editing to alter a 7 bp region in the

168 endogenous locus which includes part of HOXA2 start codon, deleting 2 bp and converting it

169 into an *Xho*I site (5'-AGGCC**ATG**-3' to 5'-CTCGA**G**-3'). We refer to this allele as *a2KO,* which

170 minimizes changes to the locus and preserves all known *cis*-regulatory elements (Fig. 1C).

171   To validate the successful abrogation of HOXA2 protein function by this mutation, we

172 compared homozygous *a2KO* embryos to a previously characterized mutant containing the

173 *neomycin* cassette (Rijli et al. 1993) (Fig. 1C-D). We refer to this published allele as the *a2neo.*

174 As with pups homozygous for *a2neo*, homozygous *a2KO* pups die within 24 hours of birth and

175 display the previously characterized 'cauliflower ear' phenotype. Importantly, *a2KO* embryos

176 also show the same duplication of PA1-derived middle ear elements that is characteristic of the

177 *a2neo* embryos at E18.5 (Fig. 1D). It is interesting to note that *a2KO* embryos do not show the

178 cleft palate defect originally observed in *a2neo* mice (Rijli et al. 1993). Our *a2neo* colony also

179 lacks cleft palate, and a complementation test intercrossing *a2KO* and *a2neo* heterozygous

180 alleles also fails to recapitulate the cleft palate phenotype. These observations may be due to

181 differences in genetic background or an off-target effect of the *neomycin* cassette disrupting

182 expression of other genes in the *HoxA* cluster. Homozygous embryos with *a2KO* or *a2neo* alleles

183 show matching phenotypes with respect to PA2 derived structures and affected tissues,

184 rendering the *a2KO* allele a valid genetic model for studying *Hoxa2* function in NCCs.

185

186 <u>PA1 and PA2 have distinct molecular states early in NCC migration</u>

187 The 'ground state' model considers that *Hoxa2* is a selector gene for PA2 fate, modifying

188 the *Hox*-free ground state observed in PA1 (Fig. 1B). Thus, we wanted to understand when

189 differences appear in the transcriptional profiles of NCCs from PA1 and PA2 during

190 development and when HOXA2 acts to modify the putative ground state to specify PA2 fates.

191 To address these questions, we dissected PA1 and PA2 from wildtype (WT) and homozygous

192 *a2KO* mutant embryos at four timepoints, ranging from early NCC migration (E9.0) to the start

193 of differentiation (E10.5), and examined their transcriptional profiles by bulk RNAseq

194 (bRNAseq). While NCCs represent the majority of cells in the dissected PA tissue, the arches

195 also contain cells from the surface ectodermal and endodermal layers and a core of

196 mesodermal cells (Fig. 1A). We utilized the entire PA tissue for these experiments to avoid

197 inducing changes in cell properties during manipulations or finer level dissections and to ensure

198 we had the full cellular repertoire of components of the PAs.

199 We first examined when molecular differences between PA1 and PA2 appear during

200 NCC migration and early differentiation by performing differential gene expression analysis

201 (Supplementary Tables S1-5). If early NCCs migrating into the PAs have a common ground state

202 that is progressively modified in PA2 by HOXA2, their initial transcriptional profiles in PA1 and

203 PA2 would be predicted to be quite similar, with differences emerging and becoming more

204 pronounced as HOXA2 exerts its activity during the course of NCC colonization of the PAs. Our

205 data reveal that early in migration at E9.0, PA1 and PA2 already display significantly different

206 transcriptional profiles and this pattern persists through E9.5 (Fig. 2A), arguing against a

207 common molecular ground state early in the developmental process. Then as the embryo

208 continues to develop from E10.0-E10.5, at the onset of NCC differentiation, we observe

209 progressively fewer differences between PA1 and PA2. The majority of the differentially

210 expressed genes are unique to a particular timepoint, although 89 genes are PA-biased

211   throughout development and a fair number of genes are differentially expressed at both E9.0

212   and E9.5, when we observe the greatest transcriptional differences between PA1 and PA2

213   (Supplementary Fig. S1A-B).

214
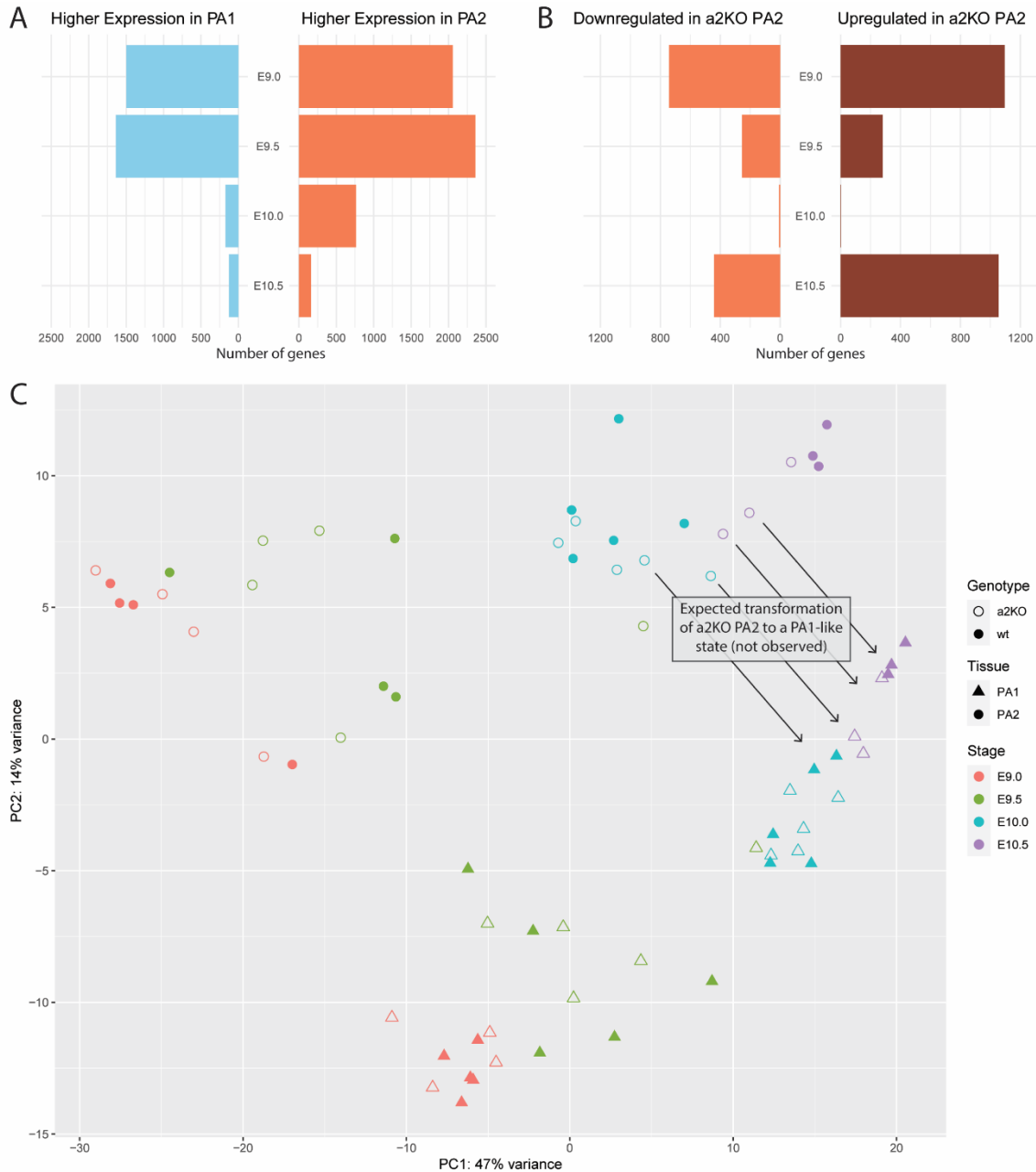
Figure 2. Hoxa2 knockout PA2 does not revert to a PA1-like transcriptional state. A) Number of genes differentially expressed between WT PA1 and WT PA2 at each timepoint E9.0-E10.5. B) Number of genes differentially expressed between WT PA2 and a2KO PA2 at each timepoint E9.0-E10.5. C) Principal component analysis (PCA) plot depicting clustering of WT PA1, WT PA2, a2KO PA1, and a2KO PA2 from E9.0-E10.5. Each point corresponds to a sample from an individual embryo (PA1 and PA2 were both collected from each embryo). Color corresponds to timepoint, shape corresponds to tissue, fill corresponds to genotype. All samples cluster according to PA of origin, with PA2 in upper left of the plot and PA1 in lower right, independent of genotype.

11
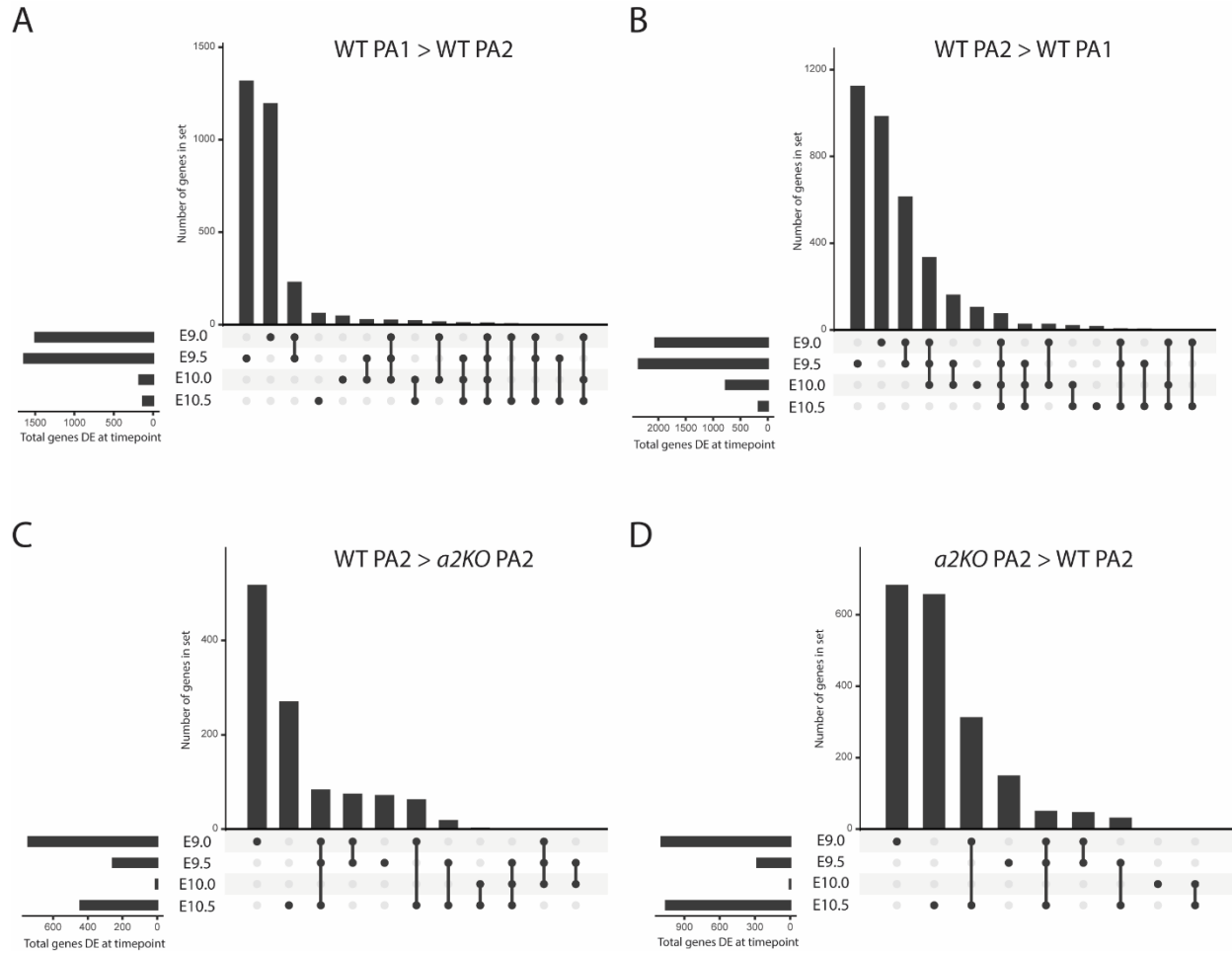
Supplementary Figure S1. UpSet plots depicting differentially expressed genes across timepoints in bRNAseq dataset. UpSet plots depict overlapping data in a clearer format than Venn diagrams. Each timepoint is listed at the left, with dots (connected by lines) showing the datasets that a given group of genes (bar) belongs to. For further information on UpSet plots, refer to (Lex et al. 2014). A) Genes with higher expression in WT PA1 than WT PA2 at any timepoint. B) Genes with higher expression in WT PA2 than WT PA1 at any timepoint. C) Genes downregulated in PA2 in the absence of HOXA2. D) Genes upregulated in PA2 in the absence of HOXA2.

234   Overall, these data indicate that cranial NCCs emerging from the hindbrain at different

235   axial levels have distinct transcriptional profiles as they begin to migrate into PA1 and PA2,

236   suggesting that axial identities may already be established by early stages of NCC migration. The

237   similarity of transcriptional profiles in both arches at later stages may reflect that NCCs are

238   undergoing differentiation programs that generate a similar repertoire of cell types -

239   osteoblasts, chondrocytes, neurons, glia, and melanocytes in each pharyngeal arch

240   environment. These cells may exist in different proportions and end up in unique orientations

241   relative to one another, ultimately resulting in distinct derivatives in PA1 and PA2, however the

242   cell types forming these structures are similar.

243

244   _Hoxa2_ maintains the molecular character of PA2 in different phases of NCC development

245   To investigate how the loss of HOXA2 affects PA2 development, we compared the

246   transcriptional profiles between PA2 of WT and _a2KO_ embryos and identified genes

247   differentially expressed during NCC migration and early differentiation (Fig. 2B and

248   Supplementary Tables S6-10). At the earliest timepoint (E9.0), there are significant

249   transcriptional differences in PA2 between WT and _a2KO_ embryos, indicating that _Hoxa2_ plays

250   an important early role in shaping PA2 identity. These molecular differences then decrease as

251   NCCs colonize the PAs (E9.5-E10.0), but then pronounced differences once again arise in their

252   expression profiles as they begin to differentiate at E10.5 (Fig. 2B). Many of the genes

253   differentially expressed between WT PA2 and _a2KO_ PA2 are specific to a particular timepoint.

254   For example, 65% of genes differentially expressed at E9.0 and 62% of genes differentially

255   expressed at E10.5 are not differentially expressed at any other timepoint (Supplementary Fig.

256   S1C-D). Thus, the loss of HOXA2 results in series of dynamic changes in the transcriptional

257   program of NCCs from PA2. Consistent with the observed _Hoxa2$^{-/-}$_ phenotype of increased

258   ossification in PA2, the genes differentially expressed at E10.5 include _Msx2_, which is expressed

259   at higher levels in _a2KO_ PA2 than WT PA2, suggesting an increase in osteogenesis. Taken

260   together, these data suggest that _Hoxa2_ has multiple roles in regulating transcriptional

261   programs in different phases of NCC development – i.e. migration and differentiation.

13

262

PA2 is not transformed to the molecular character of PA1 in the absence of *Hoxa2* activity

264   Our bRNAseq analysis indicates that the establishment and maintenance of the

265 transcriptional signature of PA2 depend upon HOXA2 (Fig. 2B). We then examined whether the

266 changes observed in the transcriptional profiles of PA2 represent a general reversion to that of

267 PA1, as predicted by the ground state model. To compare transcriptional signatures over the

268 timecourse between the WT and *a2KO* samples, we performed principal component analysis

269 (PCA) to visualize similarities and differences between their profiles (Fig. 2C). WT PA1 and PA2

270 begin by clustering separately at E9.0 and E9.5, in accordance with our observation that in

271 these early stages of NCC development, gene expression differs greatly between the two (Fig.

272 2A, C). The differences are less pronounced at the E10.0 and E10.5 timepoints. If PA2 converts

273 to a PA1-like signature in *a2KO* mutants, in association with the transformation of PA2

274 derivatives to PA1, at some point in the timecourse we expected to see *a2KO* PA2 begin to

275 cluster with PA1 of WT and *a2KO* embryos. To our surprise, the transcriptome of *a2KO* PA2

276 samples at all timepoints continues to cluster with the corresponding transcriptome of WT

277 PA2and do not at any point cluster with PA1 samples from WT or *a2KO* embryos (Fig. 2C). The

278 fact that this continues into E10.5, when gene activity has previously been shown to be altered

279 due to the absence of *Hoxa2* (Santagati et al. 2005; Donaldson et al. 2012), suggests that the

280 clear phenotypic transformation of PA2 derivatives in *a2KO* embryos is not accompanied by a

281 general transition in the transcriptional state of PA2 to that of PA1. Hence, the phenotypic

282 ground state is not reflected in an underlying common molecular ground state.

283

Single-cell transcriptomics reveals heterogeneity of PA1 and PA2 during NCC differentiation

285   One possible explanation for the observed lack of transformation at the transcriptional

286 level is heterogeneity in the tissue collected via manual dissection of PAs (Fig. 1A & 3B). While a

287 large fraction of the cells in the PAs at the stages examined are NCCs, cells from other tissues of

288 the PAs (ectoderm, endoderm and mesoderm) may make it difficult to identify NCC-specific

289 effects using whole PAs. The concerns about tissue heterogeneity and the challenges of

290   understanding tissue-specific effects of *Hoxa2* in this context led us to pursue a higher-

291   resolution technique to address these questions at the level of single cells. Because our

292   bRNAseq analysis and previously published data (Santagati et al. 2005; Donaldson et al. 2012;

293   Amin et al. 2015) support a significant contribution of HOXA2 to NCC differentiation, we

294   collected PA1 and PA2 from WT and *a2KO* embryos at E10.5 and performed scRNAseq to

295   compare gene expression at the single-cell level (Fig. 3A). As with our bRNAseq experiments,

296   we used whole PAs to maintain cell health during collection and to avoid biasing the isolation

297   process by ensuring access to a full repertoire of cellular components of the PAs. The presence

298   of non-NCC tissues also allows further interrogation of cell non-autonomous effects. After

299   filtering the data for quality, we performed an integrated analysis in Seurat v3 (Stuart et al.

300   2019) to concurrently look at all four samples (Supplementary Fig. S2). To facilitate accessibility

301   to these data, we have created and made available an R ShinyApp to visualize gene expression

302   across cells in this dataset, available at https://simrcompbio.shinyapps.io/irp_scrnaseq_2020/.

303

304
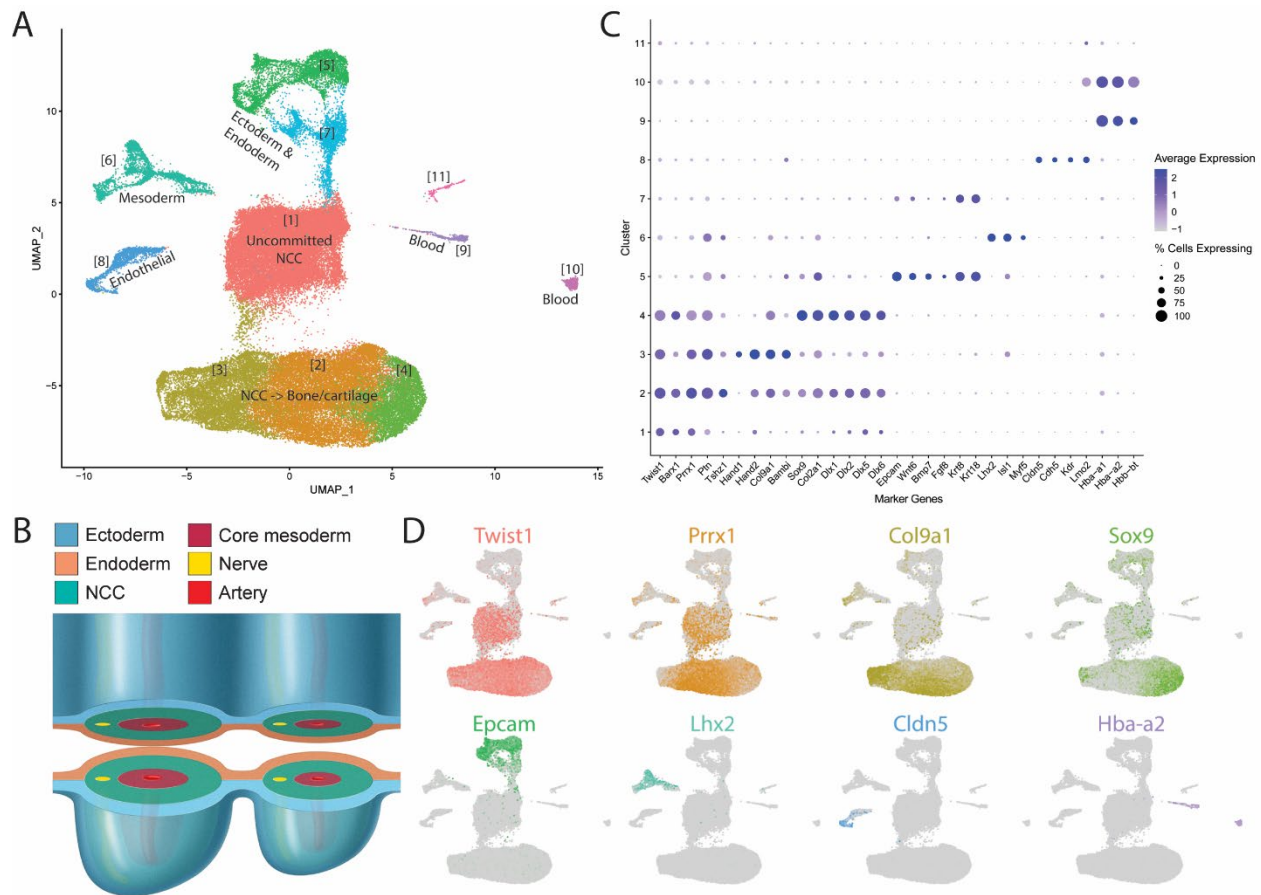
Figure 3. Single-cell RNAseq data demonstrate the heterogeneity of cells in the PAs. A) Uniform manifold approximation and projection (UMAP) depicting a total of 67,674 cells across the four samples were used for downstream analysis after quality control filtering for low sequencing depth and doublets. B) Cross-section representing key PA structures at the onset of NCC differentiation (E10.5). C) Marker gene expression allows the identification of eleven distinct clusters common to all PAs sampled. D) UMAP visualization of marker genes for selected clusters.

312

313
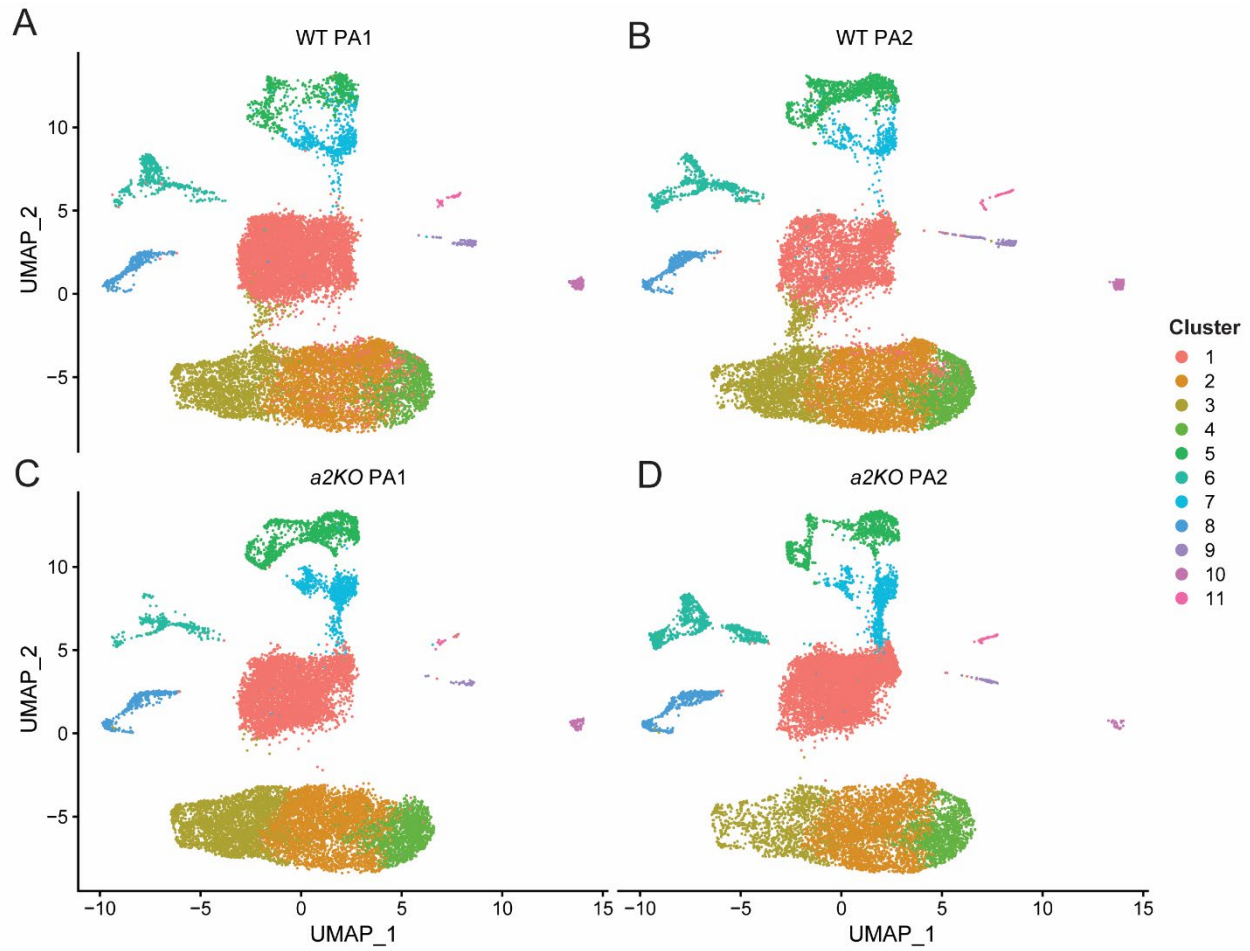
Supplementary Figure S2. UMAP visualization of cells from each of the four samples. Cells colored by cluster as defined in Figure 3. A) WT PA1. B) WT PA2. C) *a2KO* PA1. D) *a2KO* PA2.

316

317

318   Clustering the cells from all four samples results in 67,674 cells arranged in 11 clusters

319   (Fig. 3A). Based on known marker genes characteristic of tissues and cell types, we were able to

320   assign identities to the cells in each cluster (Table 1, Fig. 3C-D, Supplementary Table S11).

321   **Table 1.** Cluster identity of cells from E10.5 WT PA1, WT PA2, a2KO PA1, and a2KO PA2.

Cluster	Identity	Marker genes
1	Uncommitted NCC	Twist1, Barx1, Crabp1, Dlx6
2	NCC -> bone/cartilage	Twist1, Prrx1, Col9a1
3	NCC -> bone/cartilage	Hand1, Hand2, Col9a1
4	NCC -> bone/cartilage	Sox9, Col2a1, Dlx1, Dlx2, Barx1
5	Endoderm & ectoderm	Epcam, Wnt6, Fgf8, Bmp7
6	Mesoderm	Myf5, MyoD
7	Endoderm & ectoderm	Epcam, Wnt6, Fgf8, Bmp7
8	Endothelial	Cldn5, Kdr, Lmo2
9	Blood	Hbb-bs, Hba-a1, Hbb-bt
10	Blood	Hba-bh1, Hba-a1, Hbb-a2
11	Unknown	Pf4, Fcer1g, Tyrobp, C1qb, Lyz2

322

323   At E10.5, the majority of the cells (80.2%), represented by clusters 1-4, are of neural

324   crest origin and many of them show gene expression profiles characteristic of cells that have

325   begun to differentiate into NCC derivatives. Clusters 2-4 correspond to NCCs differentiating into

326   bone and cartilage, characterized by the expression of established marker genes such as *Sox9*,

327   *Col2a1*, *Col9a1*, *Prrx1*, *Hand1*, and *Hand2*. We also observe a population of NCCs (cluster 1) that

328   express known NCC markers, including *Twist1* and *Barx1*, but do not express genes indicative of

329   a commitment to a particular fate. These may represent a later-migrating population of NCCs

330   that have yet to initiate programs of differentiation at the time of tissue collection.

331   In addition to NCCs, we also observe populations of ectodermal and endodermal cells

332   (clusters 5 & 7), as well as pharyngeal mesoderm (cluster 6) and endothelium (cluster 8). Two

333   clusters of cells (clusters 9 & 10) are largely defined by their expression of hemoglobin genes,

334   suggesting that they are blood cells. There are several possible sources of blood cells in this

335   experiment that likely explain the presence of these two clusters - one source being

18

336   contamination picked up from the dish during PA isolation and the other corresponding to

337   blood cells developing in the PAs. Finally, there is a small cluster (11) of cells that do not

338   correspond to a known cell type. In summary, these transcriptional profiles of single cells within

339   the PAs allow us to identify populations that reflect specific tissues and cell types known to

340   reside within PA1 and PA2 of WT and *a2KO* embryos, including NCCs undergoing

341   differentiation.

342

343   <u>NCC clustering reflects spatial, temporal and cell type differences</u>

344   The scRNAseq dataset enables us to identify individual subsets of NCCs as they commit

345   to specific fates and begin to form derivative structures. The four clusters of NCCs and NCC

346   derivatives (clusters 1-4) display underlying transcriptional differences that reflect spatial,

347   temporal and cell type differences between and within PA1 and PA2. For example, looking at

348   the distribution of proximal-distal markers, we see a clear gradient through the bone and

349   cartilage derivatives (clusters 2-4). Cluster 3 contains distal NCCs marked by expression of

350   *Hand1* and *Hand2,* while cluster 4 corresponds to proximal NCCs marked by expression of *Barx1*

351   and *Pou3f3* (Fig. 4A). This data suggests a clear proximal-distal (right-left) order is reflected in

352   the clustering of NCC-derived bone/cartilage. In cluster 1, the less committed NCCs, we see

353   lower levels and greater heterogeneity in the expression of these proximal-distal markers,

354   supporting the idea that this cluster corresponds to NCCs found throughout the arch that have

355   not yet adopted a particular fate. Examining rostral-caudal markers in clusters 2-4, we see that

356   cells in the lower left are marked to a greater extent by *Gsc*, indicating a caudal bias, while cells

357   in the upper right are marked by *Lhx8*, indicative of rostral cells (Fig. 4B). Cluster 1 again shows

358   lower levels and more heterogeneous expression of rostral-caudal markers, consistent with the

359   idea that these cells cluster according to their identity as less committed NCCs rather than

360   based on a spatial location within the arches. This illustrates that clustering trends that

361   generate clusters 2-4 have captured positional information and spatial arrangements of NCCs in

362   the PAs.

363

364
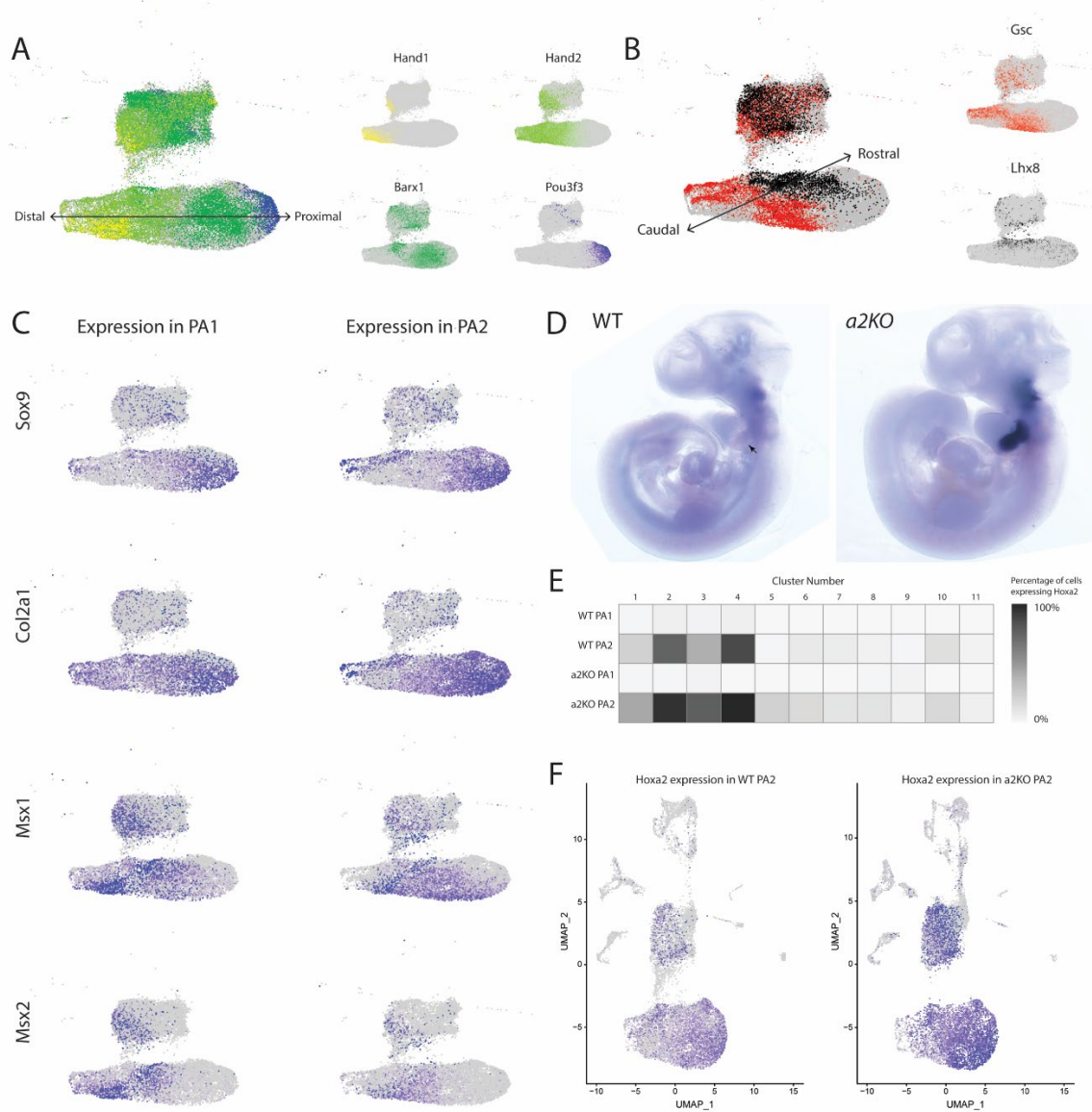
Figure 4. Spatial markers and *Hoxa2* expression delineate subsets of NCC derivatives. A) A left-right distal-proximal axis emerges in NCC-derived bone/cartilage of the PAs. *Hand1* and *Hand2* expression mark distal cells, while *Barx1* and *Pou3f3* expression mark proximal cells. B) An upper right-lower left rostral-caudal axis emerges in bone/cartilage NCC derivatives, marked by *Lhx8* (rostral) and *Gsc* (caudal) expression. C) Markers of chondrogenesis, *Sox9* and *Col2a1*, are segregated in their expression from markers of osteogenesis, *Msx1* and *Msx2*. D) *Hoxa2* expression in WT and *a2KO* mouse embryos at E10.5. D) *Hoxa2* expression in WT PA2 (left) and *a2KO* PA2 (right). *Hoxa2* transcript is still observed in a2KO PA2 due to the nature of the *a2KO* allele, in which the gene is still transcribed but the transcript cannot be translated. E) Percentage of cells in each cluster expressing *Hoxa2* transcript. F) Visualization of *Hoxa2* expression in WT PA2 (left) and *a2KO* PA2 (right) in scRNAseq data.

376   With respect to cell types, markers of chondrogenesis and osteogenesis also display a

377   fair amount of segregation (Fig. 4C and Supplementary Fig. S3). *Sox9* and *Col2a1*, hallmarks of

378   chondrogenesis, show the highest levels of expression in cluster 4, with limited expression at

379   the distal-most tip of cluster 3. We observe similar levels of expression between PA1 and PA2,

380   with a bias toward the proximal domain of the arches, consistent with previous descriptions of

381   their expression domains. In contrast, *Msx1* and *Msx2*, regulators of osteogenesis, are largely

382   expressed in cluster 2. Expression of these genes is higher in PA1 than PA2, as expected

383   considering greater intramembranous ossification in PA1 (Minoux and Rijli 2010). Moreover,

384   *Msx1* and *Msx2* expression is biased in both arches toward the distal end of the clusters,

385   consistent with their endogenous patterns of expression. This segregation and lack of overlap

386   between differentiation markers supports the observation that chondrogenesis and

387   osteogenesis are occurring in distinct groups of cells. In cluster 1, the expression of all of these

388   markers is lower and less segregated, consistent with the idea that these cells have not yet

389   committed to a bone/cartilage fate. Taken together, these transcriptional profiles reveal that

390   NCC-derived bone and cartilage cells, undergoing differentiation at E10.5, show spatial and cell

391   differentiation biases in their clustering that capture diverse endogenous features of NCCs in

392   the PAs.

393
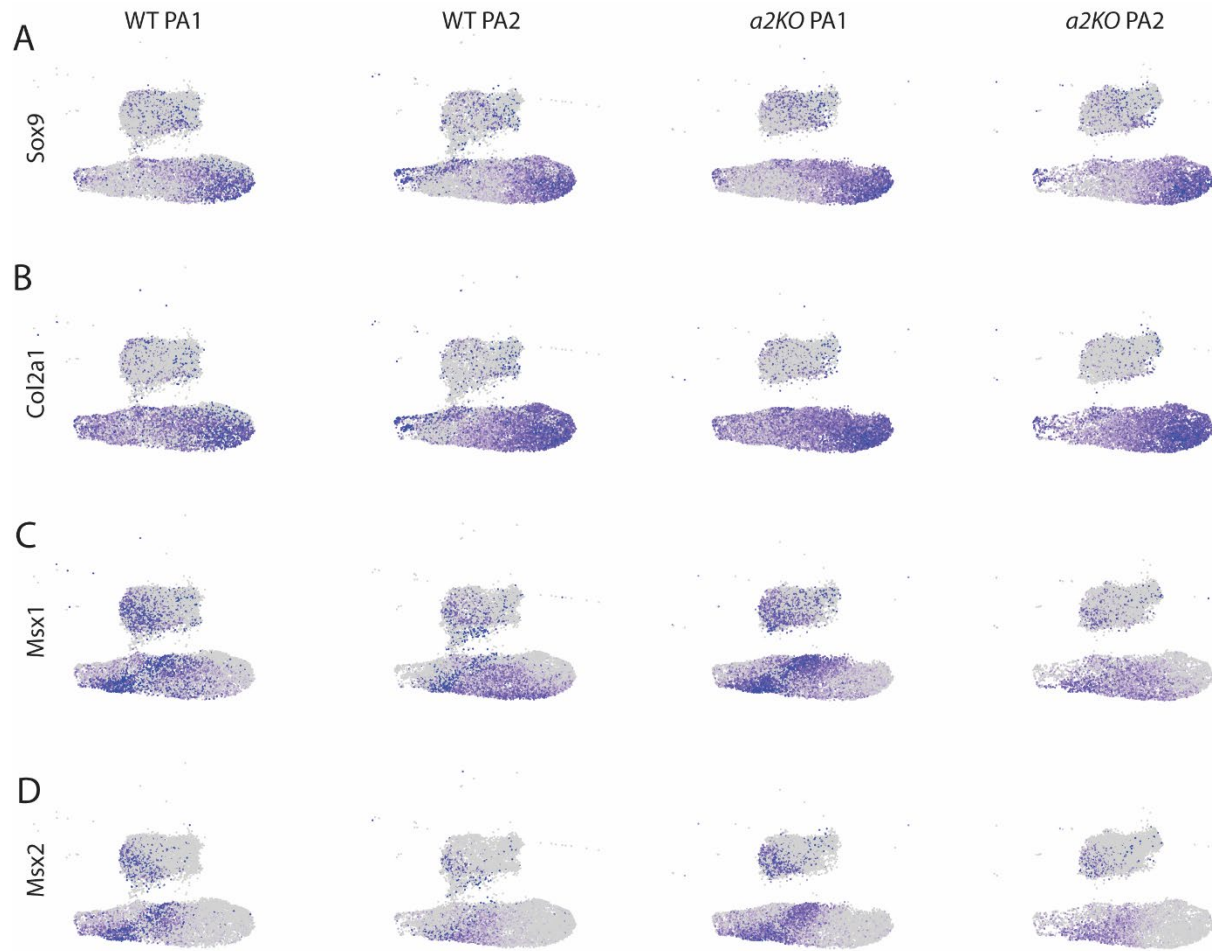
Supplementary Figure S3. Visualization of chondrogenesis and osteogenesis markers across WT and *a2KO* PA1 and PA2. A) Chondrogenesis marker *Sox9*. B) Chondrogenesis marker *Col2a1*. C) Osteogenesis marker *Msx1*. D) Osteogenesis marker *Msx2*.

399   *Hoxa2 expression is enriched in NCCs and NCC-derived clusters at E10.5*

400   To probe the role of *Hoxa2* in specifying axial identity, we next wanted to examine its

401   expression within the scRNAseq dataset. We designed the *a2KO* mutation so that the

402   homozygous mutant mice produce a *Hoxa2* transcript with a small change (7 nt) spanning the

403   initiation codon, which prevents translation. This enables us to monitor endogenous *Hoxa2*

404   transcripts in embryos of both WT and *a2KO* embryos. To validate this ability, we performed

405   whole mount in situ hybridization in E10.5 WT and *a2KO* embryos and found that *Hoxa2* is

406   expressed in identical domains in the hindbrain and PAs (Fig. 4D). Intriguingly, we observe

407   higher levels of *Hoxa2* transcripts in PA2 of the *a2KO* mutants compared to WT embryos, which

408   is consistent with levels observed in our bulk and single cell RNAseq data (Fig. 4F). This domain-

409   specific elevation of *Hoxa2* transcript levels may arise through the input of cross-regulatory

410   feedback circuits known to modulate *Hox* expression in the hindbrain and NCCs (Parker et al.

411   2019; Parker and Krumlauf 2020). The ability to monitor endogenous *Hoxa2* transcripts in *a2KO*

412   mutants is important because the expression of *Hoxa2* serves as a lineage tracer in this system

413   and indicates that these cells survive even in the absence of HOXA2. Moreover, directly

414   comparing the properties of cells expressing *Hoxa2* in WT and *a2KO* embryos enables us to

415   identify transcriptional differences associated with *Hoxa2*-dependent activity.

416   In PA1 of WT and *a2KO* embryos, which are expected to be *Hox*-negative, fewer than 5%

417   of the cells express *Hoxa2* and they are not enriched in any single cluster (Fig. 4E and

418   Supplementary Fig. S4). The low fraction of *Hoxa2*-expressing cells observed could be due to

419   contamination during the cell collection process or a small population of *Hoxa2*-expressing cells

420   in the tissue that have not been previously described. In both WT and *a2KO* PA2, we see the

421   highest levels of *Hoxa2* transcript in NCCs and NCC-derived clusters (1-4), with very few cells

422   expressing *Hoxa2* in surface ectoderm, endoderm, mesoderm or endothelia (Fig. 4F).

423   Expression of *Hoxa2* is spread throughout clusters 2-4, with higher levels of expression in

424   clusters 2 and 4 than clusters 1 and 3. The differences in expression levels in NCC clusters may

425   be related to the emerging identities and fates of these cells and the temporally dynamic roles

426   of HOXA2 on the establishment of these identities.
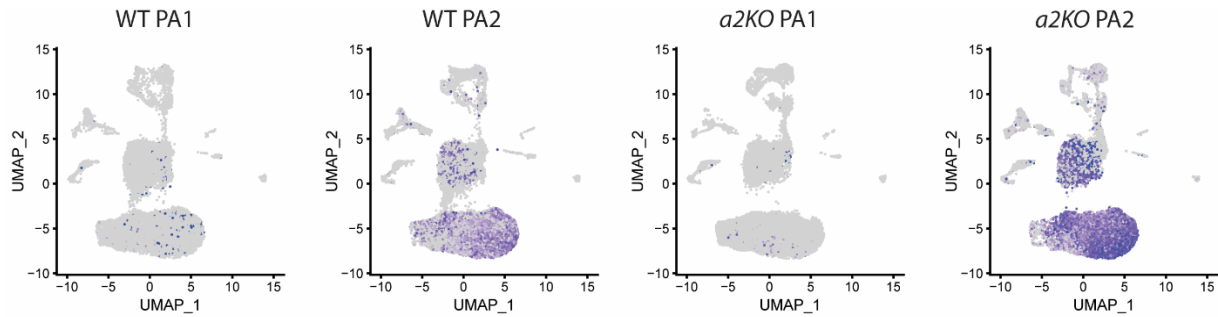
Supplementary Figure S4. Visualization of *Hoxa2* expression in WT PA1, WT PA2, *a2KO* PA1, and *a2KO* PA2.

Comparing transcriptional signatures of PA1 and PA2

We sought to leverage the richness of our bRNAseq and scRNAseq datasets to understand key characteristics that define the transcriptional states of PA1 and PA2, as well as how these states are modified in the absence of *Hoxa2*. Returning to the differential expression analysis of our bRNAseq datasets, we focused on early differentiation at E10.5 and looked at genes differentially expressed between WT PA1 and WT PA2 (Supplementary Table S12). We refer to the 126 genes more highly expressed in PA1 as the 'PA1 transcriptional signature' and the 164 genes more highly expressed in PA2 as the 'PA2 transcriptional signature' (Fig. 5A-B).

We then compared the expression of genes in these signatures between WT and *a2KO* embryos at E10.5 using the bRNAseq dataset. As expected, because *Hoxa2* is not expressed in PA1, we observe that the genes of the PA1 signature are highly expressed in both WT PA1 and *a2KO* PA1 (Fig. 5A). Interestingly, we do not see a noticeable increase in their expression in *a2KO* PA2 over WT PA2, which would be expected in a reversion of the mutant tissue to a PA1-like ground state. Equally strikingly, we see that many of the genes of the PA2 signature are likewise still strongly expressed in *a2KO* PA2 (Fig. 5B). The persistence of components of the PA2 signature and lack of induction of the PA1 signature further support the idea that there has not been a conversion of the transcriptional state of PA2 in *a2KO* embryos to a PA1-like state at this stage in association with the phenotypic transformation.

24
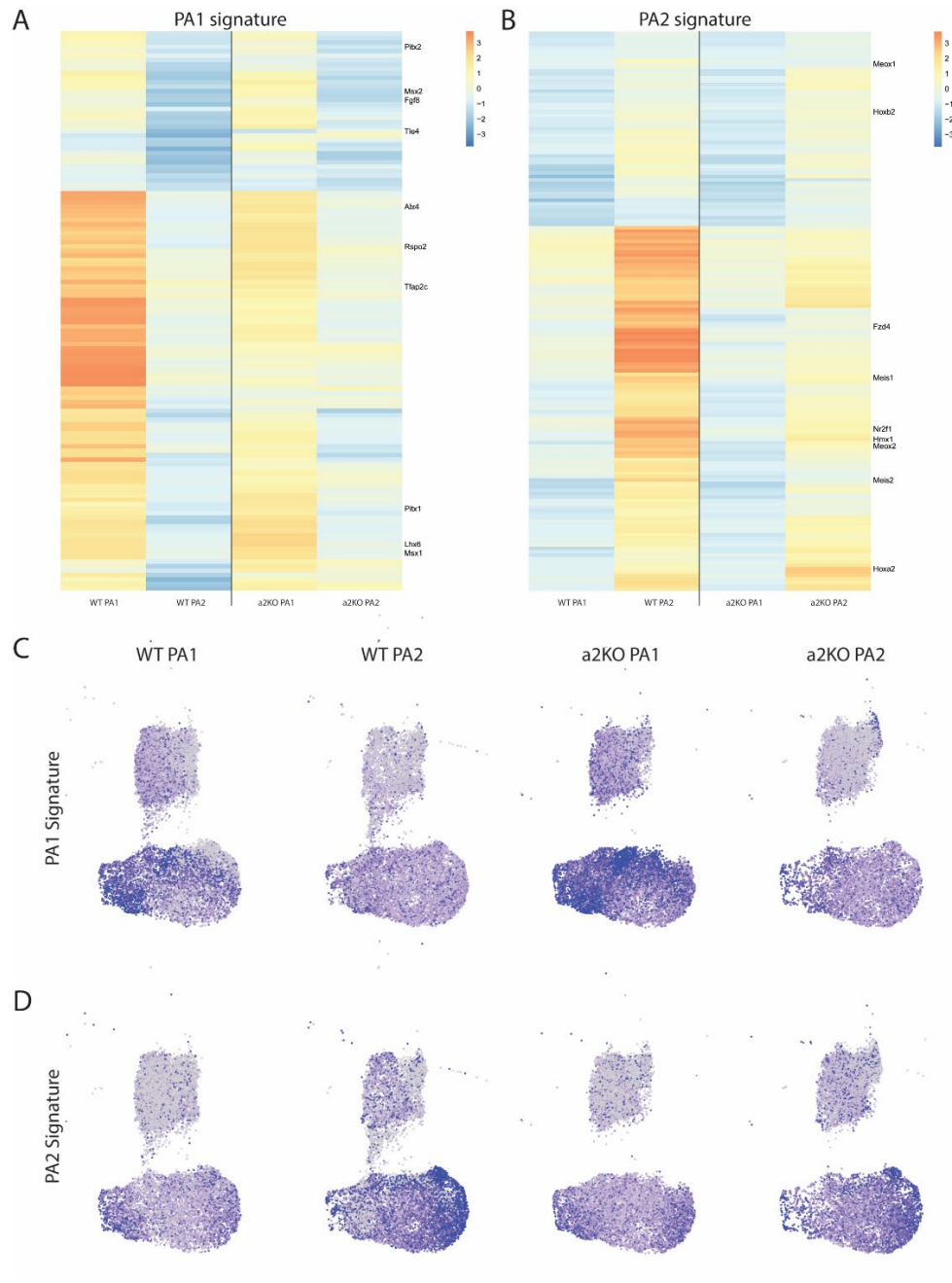
Figure 5. Transcriptional signatures of PA1 and PA2 at the onset of NCC differentiation. Differential expression analysis from bRNAseq between WT PA1 and WT PA2 at E10.5 generated a 126-gene PA1 transcriptional signature and 164-gene PA2 transcriptional signature. Visualization of these signatures across bRNAseq (A & B) and scRNAseq (C & D) E10.5 datasets across WT PA1, WT PA2, *a2KO* PA1, and *a2KO* PA2 reveals trends in transcriptional identity. bRNAseq data (A & B) shown as Z-scores of expression across all conditions and timepoints for each gene. scRNAseq data (C & D) shown as normalized expression of a MetaFeature for each PA-specific signature across NCCs in each condition.

458   The expression of these transcriptional states is consistent between the bRNAseq and

459   scRNAseq datasets. Aggregate gene expression of the PA1 signature is strongest in distal NCCs

460   (cluster 3). We again observe strong expression of these genes in both WT and *a2KO* PA1, with

461   limited expression in WT and *a2KO* PA2 (Fig. 5C). Aggregate gene expression of the PA2

462   signature is strongest in proximal NCCs (cluster 4). This expression is maintained in PA2 even in

463   the absence of HOXA2 (Fig. 5D). Taken together, these data show that the *Hoxa2-/-* phenotypic

464   reversion is not matched by a corresponding molecular transformation of PA2 to a PA1-like

465   transcriptional ground state.

466

467   Integration of transcriptomic datasets to identify putative HOXA2 targets in NCCs

468   To search for *Hoxa2*-dependent genes associated with axial specification, we identified

469   genes that are differentially expressed between PA1 and PA2 in WT embryos, as well as those

470   whose expression in PA2 changed in *a2KO* mutant embryos. For candidate genes specifying PA1

471   fate, we searched for genes that are expressed at higher levels in PA1 than PA2 of WT embryos,

472   and also for those expressed at higher levels in PA2 of *a2KO* mutant embryos (potentially

473   repressed by HOXA2) compared to WT. Conversely, for genes specifying PA2 fate, we identified

474   genes that are expressed at higher levels in PA2 than PA1 of WT embryos, and those expressed

475   at higher levels in PA2 of WT (potentially activated by HOXA2) compared to *a2KO* embryos. This

476   two-step selection strategy identifies candidate genes that are downstream of *Hoxa2* and play

477   potential roles in regulating the axial identity of NCCs.

478   To further exploit our transcriptomic datasets, we applied these criteria to both the

479   bRNAseq dataset and the NCC and NCC-derived clusters (1-4) of the scRNAseq dataset,

480   identifying 90 PA1 specifiers and 233 PA2 specifiers (Supplementary Tables S13 & S14). Among

481   PA1 specifiers identified across datasets, we observe a very strong enrichment of ribosomal

482   components and functions, including Gene Ontology (GO) terms for translation, peptide

483   biosynthetic process, and RNA processing (Supplementary Table S15). The increase in

484   expression of these components of protein synthesis in *a2KO* samples suggests they may be

485   negatively regulated by *Hoxa2*. In contrast, PA2 specifiers are strongly enriched for

26

486   transcription factors and transcriptional regulation, featuring GO terms such as protein binding,

487   *cis*-regulatory region binding, and anatomical structure development (Supplementary Table

488   S16). The decrease in expression levels of these genes in *a2KO* embryos indicates they may be

489   positively regulated by HOXA2.

490   **Table 2.** Putative *Hoxa2*-responsive axial specifiers identified through differential gene

491   expression analysis from bRNAseq and scRNAseq NCC clusters.

Hoxa2-repressed PA1 specifiers			Hoxa2-activated PA2 specifiers		
Ribosomal	*Hoxa2-repressed*	*Novel*	*Hoxa2-activated*	*Novel*	
Rpl35	Lhx6	**Prrx1**	Meox1	Pax9	**Enho**
Rpl27	Alx4	**Ift57**	**Meis1**	**Tbx15**	**Errfi1**
mt-Rnr1	**Rspo2**	**Rnd3**	**Meis2**	**Cntfr**	**Nr2f1**
mt-Rnr2	**Barx1**	Peg10	**Fzd4**	Pou3f4	Hmx1
Npm1	Pitx1	**Tle4**	**Zfp703**	**Ptn**	**Tshz1**

492

493   From candidate *Hoxa2*-responsive specifiers, some of the individual genes revealed by

494   this comparative analysis offer insight into potential downstream pathways involved in the

495   process (Table 2 and Fig. 6A-B). Among PA1 specifiers, we see a number of ribosomal subunits

496   and rRNA processing genes, including *Rpl35*, *Rpl27*, *mt-Rnr2*, and *Npm1*. We also identified

497   genes previously shown to be negatively regulated by *Hoxa2*, including *Lhx6*, *Alx4*, *Rspo2*,

498   *Barx1*, and *Pitx1* (Bobola et al. 2003; Santagati et al. 2005; Kirilenko et al. 2011; Donaldson et al.

499   2012), validating the approach. Additionally, this analysis uncovered genes of interest that have

500   not been previously characterized for their response to *Hoxa2* or their role in the specification

501   of NCC axial identity, including *Tle4*, *Rnd3*, *Ift57*, and *Peg10*. Many of the candidate PA2

502   specifiers we identified are transcription factors, including well-characterized *Hoxa2* targets

503   such as *Meis1*, *Meis2*, and *Meox1* (Kirilenko et al. 2011; Donaldson et al. 2012; Amin et al.

504   2015). In addition, some of the genes we identified as being dependent upon *Hoxa2*, are known

505   to be functionally linked with specification of NCC, including *Zfp503*, *Zfp703*, and *Fzd4*

506   (Donaldson et al. 2012). Furthermore, a number of novel targets emerged from this analysis,

27

507 including *Ptn*, *Cntfr*, *Enho*, *Errfi1*, *3110099E03Rik*, *Pou3f4*, *Hmx1*, and *Nr2f1*. Our selection

508 strategy, based on analyses of bulk and scRNAseq datasets, has identified a list of candidate

509 *Hoxa2*-responsive specifiers of NCC axial identity that include many novel and previously

510 described genes involved in NCC development.

511

512 <u>Identification of putative direct targets of HOXA2 in axial specification of NCCs</u>

513   To explore whether any of the candidate axial specifiers of PA1 and PA2 identified from

514 our analyses may be directly regulated by *Hoxa2*, we leveraged published genome-wide binding

515 data of endogenous HOXA2 protein in mouse PA2 at E11.5 (Donaldson et al. 2012). Despite the

516 difference in developmental stages, this dataset presents an opportunity for comparison of our

517 data at E10.5 with HOXA2 binding in differentiating NCCs at E11.5. In total, we find that 24/90

518 PA1 specifiers (26.7%) and 91/233 PA2 specifiers (39.1%) have at least one nearby HOXA2

519 binding peak, suggesting possible direct regulation by HOXA2 (bold in Table 2 and Fig. 6A-B). In

520 this comparison we observe that a number of genes that have been previously identified as

521 direct targets of HOXA2 show nearby binding, including putative PA1 specifiers *Barx1* and

522 *Rspo2*, as well as putative PA2 specifiers *Fzd4*, *Meis1*, and *Meis2*. However, other published

523 targets of *Hoxa2* may be indirect, as evidenced by a lack of nearby HOXA2 binding. These

524 include putative PA1 specifiers *Pitx1* and *Alx4*, as well as putative PA2 specifier *Meox1*.

525   In conclusion, this integration of DNA binding data with our analysis has allowed us to

526 identify candidate axial specifiers of NCC identity which are directly and indirectly downstream

527 of *Hoxa2* in patterning the PAs. Together, these data provide insight into the molecular

528 mechanisms and cell populations through which HOXA2 establishes the axial identity of PA2.

529

530 <u>Putative axial specifiers show diverse responses to HOXA2 activity</u>

531   To deepen our understanding of the mechanisms by which putative axial specifiers

532 uncovered through our analyses of bRNAseq and scRNAseq data impart axial identity, we

533 sought to validate our findings and explore how these genes behave across PA1 and PA2 in

534   both WT and *a2KO* embryos. We observe expression of these genes throughout the NCCs and a

535   diverse set of responses to the absence of HOXA2. *Prrx1*, a putative PA1 specifier, has been

536   shown to be essential for skeletogenesis, including correct specification of the middle ear

537   (Martin et al. 1995) but had not previously been associated with *Hox* gene expression. We

538   observe expression of *Prrx1* in PA2 of *a2KO* embryos, but not their WT littermates (Fig. 6C).

539   Putative PA2 specifiers *Nr2f1* and *Tshz1* show the converse trend – reduced expression in *a2KO*

540   PA2 when compared to WT littermates (Fig. 6D-E). *Nr2f1* has been implicated in positive

541   regulation of NCC enhancers (Rada-Iglesias et al. 2012) and the *Nr2f* family of nuclear receptors

542   has been shown to play a role in the specification of bone and cartilage in the zebrafish jaw

543   (Barske et al. 2018). *Tshz1* has been shown to play a role in middle ear development (Coré et al.

544   2007). However, neither gene has previously been shown to interact with *Hox* genes.

545   The genes identified by the comparative analyses above show unique spatial expression

546   patterns and responses to HOXA2 activity, suggesting distinct roles for these genes in *Hoxa2*-

547   mediated axial specification. The *in vivo* observations also help to validate the differential

548   association of these putative targets with specific subsets of NCCs in clusters 1-4 uncovered by

549   our datasets (Fig. 6A-B and Supplementary Tables S13 and S14). We believe that many other

550   genes identified in our comparative analysis share similar properties and with thorough

551   functional validation will enhance our understanding of *Hox*-mediated NCC axial specification.

552   In contrast to what might be expected based on the observed phenotypic transformation in

553   *Hoxa2* mutants, we conclude that there is not a singular molecular ground state in NCCs that is

554   dramatically switched by HOXA2 to impart a PA2 fate. Rather, we see different transcriptional

555   profiles for PA1 and PA2 with subsets of NCCs expressing distinct sets of genes in each PA.

556   Moreover, we see that many of the putative axial specifiers identified here do not depend upon

557   HOXA2 in all NCCs but rather show marked differences in subsets of cells. This suggests that

558   subsets of cells are likely to be responsible for imparting specific cell fates and morphogenic

559   features in the PAs (Fig. 6F). This context dependent role for HOXA2 uncovers complexity in our

560   understanding of NCC axial specification and highlights an unexplored heterogeneity of the

561   system.

29
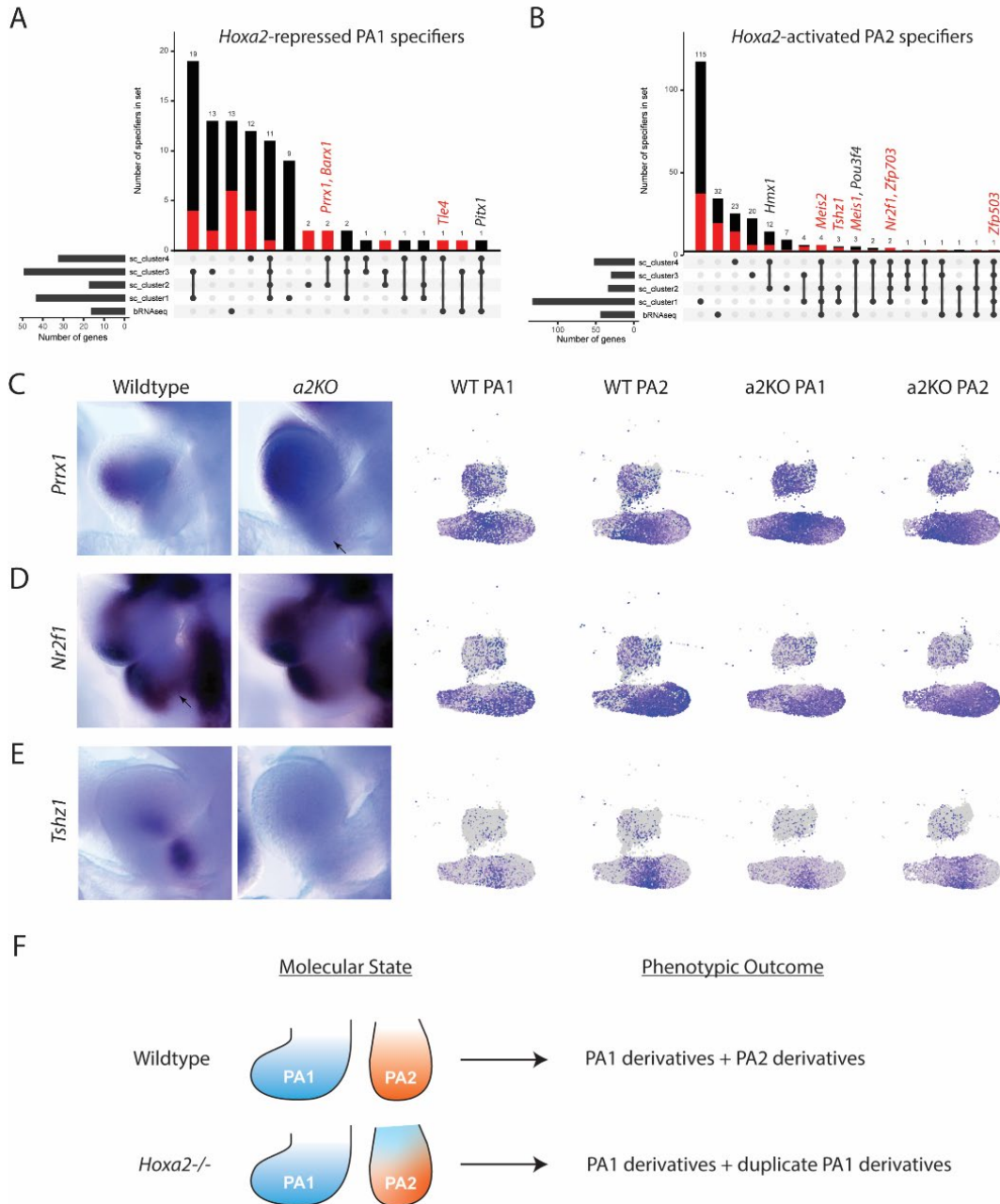
Figure 6. Putative axial specifiers show heterogeneous responses to Hoxa2 activity. A & B) UpSet plots depicting putative axial specifiers from bRNAseq and scRNAseq clusters 1-4. Red bars and text refer to putative direct targets of HOXA2 – those with nearby HOXA2 binding (Donaldson et al. 2012). A) *Hoxa2*-repressed PA1 specifiers. B) *Hoxa2*-activated PA2 specifiers. C-E) *In situ* hybridization and FeaturePlots showing expression in scRNAseq data for each gene in WT and *a2KO* embryos at E10.5, focusing on PA1 and PA2. C) PA1 specifier *Prrx1* shows expression in PA2 of *a2KO* embryos. PA2 specifiers *Nr2f1* (D) and *Tshz1* (E) show reduced expression in PA2 of *a2KO* embryos. F) Summary illustrating that the molecular state of PA2 does not correlate with the phenotypic outcome of PA2 in *a2KO* mutants.

30

572   **Discussion**

573   *Hox* genes play a key role in craniofacial development by specifying the axial identity of

574   neural crest cells migrating into the pharyngeal arches of the developing head. In this study, we

575   have used genomic approaches to investigate the transcriptional programs that underlie the

576   role of *Hoxa2* in specifying the fate of PA2 NCCs. *Hoxa2* is believed to be a selector gene that

577   serves as a regulatory switch to convert a PA1 ground state into a unique PA2 identity.

578   Comparing the bulk and single cell transcriptomes of PA1 and PA2 in wildtype and *Hoxa2*

579   mutant embryos during NCC migration and differentiation, we find that the phenotypic

580   transformations observed in *Hoxa2* mutants is not matched by a corresponding molecular

581   transformation of PA2 to a PA1-like transcriptional ground state. This separation of phenotypic

582   and molecular states has significant implications for our understanding of NCC biology and

583   craniofacial development. The scRNAseq analyses also reveal heterogenous expression patterns

584   in NCC populations within the PAs and the changes observed upon loss of HOXA2 suggest that

585   different subsets of NCCs may respond to HOXA2 activity in distinct manners related to their

586   ultimate fate. Our findings raise a number of interesting issues important for understanding

587   axial specification of NCCs and the role of HOXA2 in this process.

588   <u>Transcriptional analysis suggests that there is not a molecular NCC ground state</u>

589   Previous work has demonstrated the existence of a phenotypic 'ground state' among

590   NCCs colonizing the PAs in the developing mouse embryo, which is modified by *Hox* gene

591   expression to produce axial-specific derivatives (Minoux et al. 2009). In this study, we set out to

592   understand the molecular underpinnings of this phenotypic ground state and identify the

593   mechanisms by which *Hox* genes impart axial identity. To address this question, we began by

594   comparing WT and *a2KO* PA1 and PA2 transcriptional profiles throughout NCC migration and

595   differentiation (E9.0-E10.5). In WT embryos, we observe large differences in gene expression

596   profiles between PA1 and PA2 from the earliest point in our timecourse – E9.0, when NCCs are

597   migrating into the PAs (Fig. 2A). Hence, NCCs migrating into different PAs do not appear to

598   emerge from the neural tube with a common or shared transcriptional signature that is

599   progressively modified to generate unique axial identities. This contrasts with what might be

31

600 expected from populations of cells known to maintain plasticity and be highly responsive to

601 environmental signals as they migrate at E9.0 (Trainor and Krumlauf 2000a; Trainor and

602 Krumlauf 2000b; Schilling et al. 2001). Because the cells entering the PAs have distinct gene

603 expression patterns based on their axial level of origin prior to delamination (Hindbrain *Hox*

604 code in Fig. 1B), and have been previously shown to be primed to respond to different

605 environmental cues in the PAs (Trainor and Krumlauf 2001; Trainor et al. 2002), it is not

606 unreasonable to expect their gene expression profiles will differ during early phases of

607 migration.

608 In comparing the transcriptomes of PA1 and PA2 in both WT and *a2KO* embryos, the

609 existence of a molecular ground state underlying the previously described phenotypic

610 transformation of PA2 to a PA1 identity would suggest that the transcriptome of PA2 reverts to

611 a PA1-like transcriptome in *a2KO* embryos, mirroring the phenotypic reversion. We did not

612 observe such a transformation or switch in the molecular identity of NCCs in PA2 over the

613 course of their migration and differentiation (Fig. 2C). This argues against the existence of a

614 common PA1-like molecular ground state in NCC development that is modified by *Hox*

615 expression. The comparison of WT PA1 and *a2KO* PA1 also revealed a surprising number of

616 differentially expressed genes (Supplementary Fig. S5 and Supplementary Tables S17-21). This is

617 unexpected, as *Hoxa2* is not thought to be expressed within the NCCs giving rise to PA1

618 derivates (Couly et al. 1998) and no phenotypes in PA1 structures have been observed in

619 *Hoxa2* mutant embryos (Gendron-Maguire et al. 1993; Rijli et al. 1993). These differences in the

620 molecular character of PA1 generated by the loss of *Hoxa2* may reflect an unexpected early role

621 for the gene in modulating properties of NCCs in the hindbrain before they emigrate to colonize

622 PA1. Alternatively, the differences could be a consequence of altered signaling between PAs in

623 mutant embryos or reflect previously undetected expression of *Hoxa2* in PA1 NCCs. In this

624 regard, it is worth noting that our scRNAseq data suggest the presence of a small number of

625 *Hoxa2* expressing cells in PA1 (Supplementary Fig. S4). Regardless of the underlying

626 mechanism, this unexpected effect on gene expression in PA1 upon loss of HOXA2, reveals

627 complexities in the establishment of the PA1 transcriptional signature that are not consistent

628 with a molecular ground state model.

629
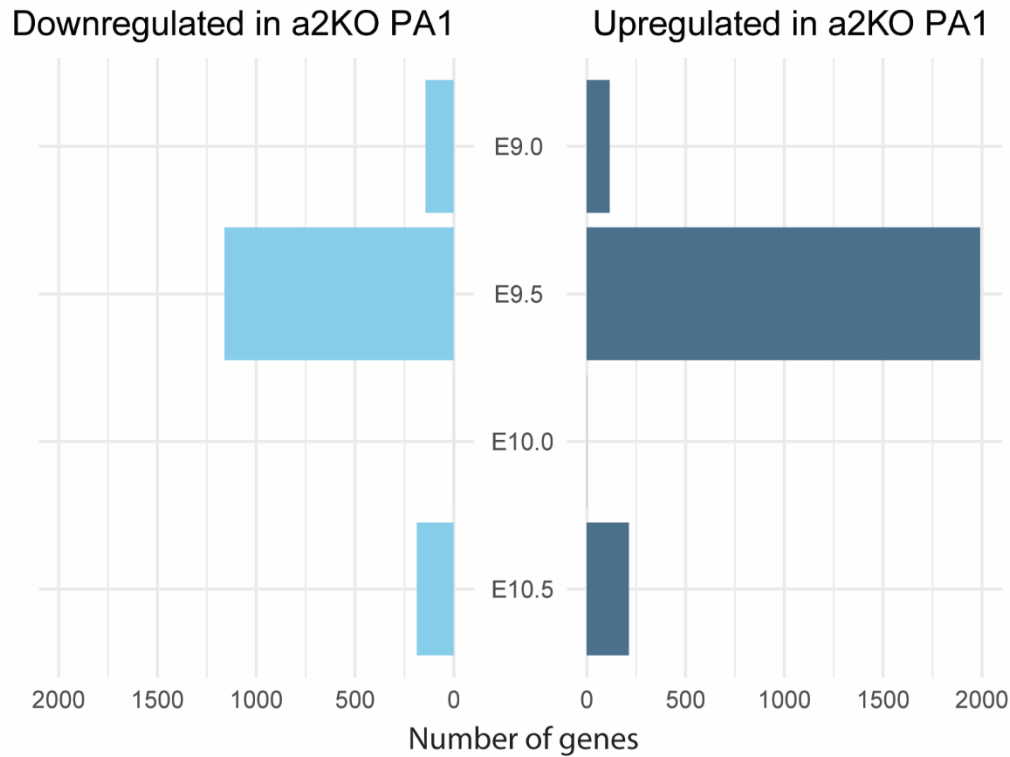
Supplementary Figure S5. Bar plot showing genes differentially expressed in bRNAseq between WT PA1 and *a2KO* PA1 across timepoints.

In considering alternatives to a ground state model, one concern in studying a heterogeneous sample, such as the PA, using bRNAseq is the noise inherent in the system, with gene expression changes potentially amplified or lost for our tissue of interest (NCCs) because of reads from another tissue. It is possible that a small set of cells, or a small set of genes are responsible for the phenotypic transformation observed in *a2KO* PA2, which would not shift the general transcriptome of the entire PA. Consistent with this idea, previous work indicates that different cells may respond to *Hoxa2* expression in different ways – with distinct requirements for levels and timing of *Hoxa2* expression within NCCs (Ohnemus et al. 2001; Santagati et al. 2005).

644   scRNAseq reveals heterogeneity of differentiating NCC populations in the mouse embryo

645   In recent years, scRNAseq experiments have been used to shed light on the dynamics of

646   embryonic development, from whole-embryo studies (Cao et al. 2019; Soldatov et al. 2019) to

647   in-depth characterization of particular developmental processes (Xu et al. 2019; Tambalo et al.

648   2020). Here, we took advantage of this approach to explore the heterogeneity of the PAs and

649   characterize the role of HOXA2 in imparting PA2 NCC identity at single-cell resolution. We

650   focused our analysis on E10.5, the start of NCC differentiation, due to the strong effects of

651   HOXA2 observed in our bRNAseq analysis and previous work characterizing HOXA2 activity at

652   this timepoint (Santagati et al. 2005; Donaldson et al. 2012; Amin et al. 2015). We generated

653   transcriptional profiles for 67,674 cells across our four samples (PA1 and PA2 from WT and

654   *a2KO* embryos), which aligned into 11 clusters, four of which correspond to NCCs. We focused

655   primarily on uncommitted NCCs (cluster 1) and NCC-derived bone and cartilage (clusters 2-4),

656   which together comprise 80.2% of the total cells isolated.

657   Our data show strong patterns in the expression of both proximal-distal and rostral-

658   caudal markers in clusters 2-4 consistent with previously published observations (Xu et al.

659   2019). This suggests that the clustering, a reflection of transcriptional similarity between cells,

660   is informed by the location of NCCs within the PA (Fig. 4A-B). Moreover, the expression of

661   chondrogenic markers *Sox9* and *Col2a1* is similar between WT PA1 and PA2, while osteogenic

662   markers *Msx1* and *Msx2* are enriched in PA1 (Fig. 4C), consistent with the formation of cartilage

663   in both tissues but bone primarily in PA1 (Dash and Trainor 2020). This trend is consistent in

664   *a2KO* embryos (Supplementary Fig. S3), implying that intramembranous ossification is not

665   increased in *a2KO* PA2 at this point in development, although it likely is at a later point as

666   duplicate PA1 bone structures are being formed in the arch.

667   Consistent with previous observations, we see *Hoxa2* expression throughout PA2,

668   expressed primarily in NCCs and NCC-derived clusters (Fig. 4D-F). It is important to note that

669   because of the structure of the *a2KO* mutant allele, *Hoxa2* transcript is produced in the

670   homozygous null embryos, but not translated. This serves as a lineage tracer for *Hoxa2*-

671   expressing cells and shows they are not lost in *a2KO* embryos, demonstrating that HOXA2 is not

34

672   required for their survival. Interestingly, we do not observe strict segregation of *Hoxa2*-

673   expressing cells and *Sox9*-expressing cells (Kanzler et al. 1998). This is potentially due to the

674   collection of these cells early in the differentiation process, a pattern that is refined over the

675   course of developmental time. The higher levels of *Hoxa2* expression at the proximal end of the

676   NCC-derived bone/cartilage clusters are also consistent with previous observations that the

677   proximo-caudal portions of PA2 require higher levels of HOXA2 for proper skeletal development

678   (Ohnemus et al. 2001).

679

680   <u>Behavior of PA-specific transcriptional signatures in WT and *a2KO* embryos indicates lack of a</u>

681   <u>molecular NCC ground state</u>

682   Based on bRNAseq transcriptomes of PA1 and PA2 in WT embryos at E10.5, we utilized

683   differential expression analysis to identify a set of genes enriched in PA1, referred to as the PA1

684   transcriptional signature, and a set of genes enriched in PA2, referred to as the PA2

685   transcriptional signature. By establishing a reference set of genes characteristic of each PA in

686   WT embryos, we provided a framework for comparison to determine how tissue identity

687   changes in the absence of HOXA2. We also used this as a reference to shed light on the

688   molecular mechanisms of HOXA2 activity and characterize the molecular underpinnings of the

689   *Hox*-free PA1 phenotypic ground state and how it is altered in $Hoxa2^{-/-}$ embryos.

690   Based on the phenotypic transformation of PA2 NCC derivatives to duplicate PA1

691   structures in the absence of HOXA2 (Minoux et al. 2009), we expect an accompanying

692   transformation of the *a2KO* PA2 transcriptome to a PA1-like molecular ground state. However,

693   the PA1 and PA2 signatures in both our bRNAseq and scRNAseq datasets revealed a retention

694   of the general PA2 signature and a lack of upregulation of PA1 signature genes in PA2 of *a2KO*,

695   embryos (Fig. 5). These data strongly suggest the absence of a true molecular NCC ground state

696   that is globally altered by *Hoxa2* expression in PA2 NCCs. The resolution afforded by scRNAseq

697   in this context enables us to identify transcriptional changes regardless of potential tissue

698   heterogeneity and noise and illustrates its value in evaluating models surrounding the

699   molecular basis of developmental and evolutionary phenotypes.

700   Our observations are consistent with a published comparison of mouse NCCs at E10.5

701   from WT PA1, WT PA2, and PA1 with ectopic *Hoxa2* expression (Minoux et al. 2017). In that

702   study, *Hoxa2* expression alters the PA1 transcriptional profile, but *Hoxa2*-expressing PA1 NCCs

703   do not cluster with WT PA2 cells, as would be expected if HOXA2 was sufficient to drive a

704   molecular transformation corresponding to the phenotypic one (Kitazawa et al. 2015). The

705   effects of HOXA2 in PA2 specification appear to be more subtle than expected, giving a glimpse

706   into what appears to be a complex regulatory picture consisting of cross-regulation with other

707   *Hox* genes (Tümpel et al. 2007), cofactors such as *Pbx* and *Meis* (Amin et al. 2015; Parker et al.

708   2019), axial signaling programs such as FGF (Trainor et al. 2002), and epigenetic regulation

709   (Minoux et al. 2017). Although the effect of *Hoxa2* knockout (Fig. 2C & Fig. 5) or overexpression

710   (Minoux et al. 2017) on the average transcriptome of NCCs is limited in scope, it nevertheless

711   results in a dramatic phenotypic transformation. Our scRNAseq dataset reveals that subsets of

712   *a2KO* PA2 NCCs do show reduction in expression of PA2 signature genes and upregulation of

713   PA1 signature genes, suggesting that a molecular transformation may be occurring on a limited

714   scale. This prompted us to further investigate the heterogeneity of NCCs and their response to

715   HOXA2.

716

717   <u>HOXA2 imparts PA2 identity in subsets of NCCs</u>

718   Several studies have now looked at transcriptional differences between PA1 and PA2 in

719   mouse embryos at various stages, seeking to identify key characteristics and components in

720   establishment of axial identity (Brunskill et al. 2014; Lumb et al. 2017; Minoux et al. 2017).

721   Other studies have identified a small set of genes regulated by *Hoxa2* within NCCs (Kanzler et

722   al. 1998; Santagati et al. 2005; Kirilenko et al. 2011; Donaldson et al. 2012; Minoux et al. 2013).

723   Despite these extensive efforts and the known role of HOXA2 in specifying NCC axial identity,

724   the link between HOXA2 activity and PA2 fate has not been well characterized at this point.

725   Here, we identified *Hoxa2*-responsive axial specifiers for both PA1 and PA2. In addition to

726   finding a number of novel candidates, several of the genes we identified have been previously

727   shown to have an axial-specific bias and others to respond to HOXA2 activity. Our analyses

728   describing putative *Hoxa2*-responsive axial specifiers establish new regulatory links between

729   these genes and the regulatory network governing the specification of NCC identity. This

730   provides functional and mechanistic insights into the role of HOXA2 in the establishment of NCC

731   axial identity.

732   PA1 specifiers are strongly enriched for translation and related processes

733   (Supplementary Table S15). There is increasing evidence from studies on craniofacial

734   abnormalities in humans and vertebrate model systems that it is important to maintain the

735   proper balance of ribosome biogenesis in cranial NCCs (Dixon et al. 2006; Jones et al. 2008;

736   Weaver et al. 2015; Terrazas et al. 2017; Watt et al. 2018). Moreover, individual genes such as

737   *Npm1* that emerge as putative HOXA2-repressed PA1 specifiers have been implicated in

738   processes including epithelial-to-mesenchymal transition, such as that observed when NCCs

739   delaminate from the neural tube to begin migration (Prakash et al. 2019). In contrast, PA2

740   specifiers are largely enriched for developmental processes and morphogenesis, with many of

741   the identified genes acting as transcription factors (Supplementary Table S16). It is encouraging

742   that we identify genes previously implicated in NCC-related processes, such as *Nr2f1* (Fig. 6D),

743   as well as genes shown to play a role in middle ear development, such as *Tshz1* (Fig. 6E), which

744   have not previously been connected to *Hox* gene activity. These connections enable us to

745   identify specific developmental processes through which *Hoxa2* likely acts to impart PA2

746   identity.

747   The differences observed between specifiers of PA1 and PA2 likely speak to the

748   processes occurring at different axial levels at this time. The enrichment for ribosomal

749   components in PA1 may suggest higher levels of proliferation in this tissue, a hypothesis

750   supported by the fact that the skeletal structures derived from PA1 NCCs are significantly larger

751   than those in PA2, thus requiring a greater expansion of the NCC population. Moreover, there

752   may be differences in developmental timing between PA1 and PA2, with PA1 forming earlier

753   than PA2, resulting in the gene expression differences observed in our data.

754   The advent of genomic tools to address questions in developmental biology marks a

755   shift in our approach to characterizing phenotypes and the activity of individual genes. These

756   data provide opportunities to explore the correlation, or lack thereof, between phenotypic

757   effects and the underlying transcriptional differences that lead to them. Studies are beginning

758   to emerge that draw a distinction between morphological and molecular phenotypes (Dooley et

759   al. 2019). Likewise, here we show that the striking phenotypic ground state of mouse NCCs is

760   nonetheless not accompanied by a corresponding molecular ground state (Fig. 6F). In light of

761   the differences we observe in transcriptional regulation between subsets of NCCs, it would be

762   invaluable to determine whether there are corresponding changes in HOXA2 occupancy within

763   the genome that correlate with them. Though we integrated a previously published dataset of

764   HOXA2 binding in PA2 (Donaldson et al. 2012), the rapid development of low-input, high-

765   resolution methods to assay transcription factor binding such as Cut & Run (Hainer and Fazzio

766   2019) and ChIPmentation (Schmidl et al. 2015) will likely prove a meaningful step toward

767   identifying such correlations at higher resolution and with more confidence. Furthermore,

768   recent data show strong epigenetic differences between craniofacial tissues across axial levels

769   (Minoux et al. 2017). The relationships between these *cis*-regulatory features, HOXA2 binding,

770   and the transcriptional status of subsets of NCCs will provide a wealth of data toward

771   understanding axial-specific processes.

772

Materials and Methods

Mouse husbandry and embryo collection

All mouse work was performed in the Laboratory Animal Services Facility at the Stowers Institute for Medical Research under IACUC approved protocols RK-2016-0164 and RK-2019-094. Euthanasia procedures were performed in accordance with recommendations by the American Veterinary Medical Association. All mice used in this study were maintained on a CBA/Ca/J x C57BL/10 background.

CRISPR-Cas9 mutation to create Hoxa2-ATG-XhoI mouse line

A CRISPR-Cas9 gene editing approach was developed to mutate a 7 bp region including part of the start codon of HOXA2 (5'-AGGCC**ATG-3'**), by deleting 2 bp and converting it into an XhoI site (5'-CTCGA**G-3'**) – hereafter referred to as the *a2KO* allele. A chimeric guide RNA was designed to target the start codon of HOXA2, consisting of the oligos 5'-CACCGCCGAGGGGGCTCCAAGGAGA-3' and 5'-AAACTCTCCTTGGAGCCCCCTCGGC-3', which were annealed and ligated into the pX330 plasmid (Cong et al. 2013). Together with a homology oligo (5'-CTTGCCCCCCCAAAGCCCCTCCAAAAGAGGGAACTTTTCCTCCGAGGGGGCTCCAAGGAGA**CTCGAG**AATTACGAATTTGAGCGAGAGATTGGTTTTATCAATAGCCAGCCGTCGCTCGCTGAGTGC-3'), the pX330 plasmid was microinjected into one-cell CBA/Ca/J x C57BL/10 embryos collected from superovulated donor mice. The next day, surviving two-cell embryos were transferred into pseudopregnant CBA/Ca/J x C57BL/10 females and genotyped upon weaning. Founders were maintained on this background.

Bulk RNAseq preparation and sequencing

Embryos were collected from heterozygous *a2KO* matings at approximately E9.0, E9.5, E10.0, and E10.5, with the day of identification of a vaginal plug defined as E0.5. The number of somite

39

799 pairs were counted to more accurately stage each embryo and their yolk sacs used to

800 determine genotype. To minimize variation in staging between individual embryos, we

801 narrowly defined the number of somites appropriate for each stage (E9.0: 16-17 somites, E9.5:

802 22-24 somites, E10.0: 28-29 somites, E10.5: 35-36 somites) and only used wildtype (WT) or

803 homozygous *a2KO* mutant embryos falling within the respective ranges. PA1 and PA2 were

804 individually isolated from each embryo by manual dissection in ice-cold phosphate-buffered

805 saline (PBS), flash frozen in liquid nitrogen, and then stored at -80 ^{o}C. Following genotyping,

806 Ambion TRIzol (catalog number 15596026) was added to each frozen sample, vortexed to

807 homogenize, and the Zymo Research Direct-zol mini-prep kit (catalog number R2052) with on-

808 column DNase treatment was used to extract RNA. This was performed for PA1 and PA2 of

809 individual embryos, resulting in 3-5 WT and *a2KO* biological replicates at each developmental

810 timepoint.

811 RNA quantification and quality control were performed using an Agilent 2100 Bioanalyzer. All

812 samples had RIN scores >9.0. The Takara Clontech SMART-seq v4 ultra low input RNA kit

813 (catalog number 634891), Illumina Nextera XT Library prep kit (catalog number FC-131-1096),

814 and Illumina Nextera XT Index kit (catalog number FC-131-2001) were used for polyA-selected

815 cDNA preparation and library construction. Library quality was checked using an Agilent 2100

816 Bioanalyzer, then pooled and loaded onto five lanes of an Illumina HiSeq flow cell to sequence

817 50 bp single reads for a total of 20-30X genomic coverage.

818

819 Bulk RNAseq data analysis

820 Reads were aligned to mm10 (Ensembl 91) using Tophat 2.1.1 (Kim et al. 2013). Downstream

821 analysis was performed in R 3.3.2 using EdgeR quasi-likelihood pipeline 1.4.1 (Chen et al. 2016)

822 for differential expression analysis with default settings. Differentially expressed genes between

823 samples were called with adjusted $p < 0.05$.

824

825

826   Single-cell RNAseq preparation and sequencing

827   Homozygous *a2KO* mutant embryos do not display obvious morphological phenotypes at E10.5

828   that would enable them to be distinguishable from wildtype or heterozygous littermates.

829   Hence, it was necessary to develop a rapid genotyping method to identify wildtype and

830   homozygous *a2KO* embryos which is also compatible with subsequent processing steps for

831   scRNAseq experiments. Mouse embryos were collected with their extra-embryonic membranes

832   intact at E10.5 from *a2KO* heterozygous matings and kept in Tyrode's Solution (8.0g NaCl, 0.2g

833   KCl, 0.2g $CaCl_2$, 0.21g $MgCl_2*6H2O$, 0.57g $NaH_2PO_4*H_2O$, 1.0g glucose, 1.0g $NaHCO_3$ per 1L

834   DEPC treated H_2O, pH 7.4) at room temperature until ready to proceed with dissections of the

835   PAs. Approximately 1 mm^2 piece of the yolk sac was collected for each embryo and genotyped

836   using ThermoFisher Phire Tissue Direct PCR Master Mix Kit (catalog number F170S) to rapidly

837   identify homozygous *a2KO* embryos. WT embryos were collected at E10.5 from CBA/Ca/J x

838   C57BL/10 matings.

839   PAs from homozygous *a2KO* (n = 5) and WT (n = 6) embryos were manually dissected in ice-cold

840   DEPC-treated phosphate-buffered saline (DPBS, Sigma catalog number D8537). Individual PAs

841   were pooled into four samples (WT PA1, WT PA2, a2KO PA1, a2KO PA2) and pooled samples

842   dissociated by incubation in 0.25% Trypsin + EDTA (Gibco catalog number 25200-056) for 3

843   minutes with two rounds of manual disruption by pipetting. The reaction was stopped with

844   fetal bovine serum and samples were washed two times in DPBS. Single-cell suspensions were

845   loaded on a Nexelome Cellometer Auto T4 to assess cell count and viability. All samples had

846   >90% viability and were loaded on a 10X Chromium Single Cell Controller. Libraries were

847   prepared using the Chromium Single Cell 3' Reagents Kits v3 (CG000183 Rev A). Library quality

848   was checked on an Agilent 2100 Bioanalyzer, then pooled and loaded onto two Illumina

849   NovaSeq S1 flow cells to sequence paired reads consisting of: 28 bp cell barcode & UMI, 8 bp i7

850   index, and 91 bp read. All samples were sequenced to a read depth >60,000 reads/cell.

851

852

853

41

854 **Single-cell RNAseq data analysis**

855 Reads were aligned to mm10 (Ensembl 98) using CellRanger 3.0.0. Downstream analysis was

856 performed in R 3.5.2 using Seurat 3.1.0 (Butler et al. 2018; Stuart et al. 2019). Cells were

857 removed from analysis if they had mitochondrial percentage greater than 5% or fewer than 200

858 genes expressed. DoubletFinder 2.0 (McGinnis et al. 2019) was used to remove ~20% of cells

859 identified as doublets (based on extrapolation of 10X Chromium reported multiplets for a given

860 number of recovered cells). After this final filtering step, a total of 67,674 cells remained for

861 downstream analysis. Further analysis was performed on these cells using the standard Seurat

862 Integration pipeline, with 2000 variable features and 40 principal components used for uniform

863 manifold approximation and projection (UMAP) and clustering (at resolution = 0.5). Cluster

864 identity was assigned based on marker genes identified using FindAllMarkers() function with a

865 minimum of 10% of cells expressing a gene and log fold change greater than 0.25, using marker

866 genes annotated in (Cao et al. 2019). Exploration of cell spatial distribution was performed via

867 analysis of genes described in (Xu et al. 2019). To identify genes differentially expressed

868 between samples, the FindMarkers() function was used on a cluster-by-cluster basis to make

869 pairwise comparisons between samples, with a minimum of 10% of cells expressing a gene and

870 log fold change greater than 0.10.

871

872 **Gene ontology and pathway analysis**

873 For lists of genes of interest, gProfiler g:GOSt functional enrichment analysis was used to obtain

874 GO, KEGG, and other functional characterization in R3.6.1 using gprofiler2 version 0.1.9 with a

875 statistical significance threshold of $p < 0.05$. Further information on gProfiler methodology is

876 described in (Raudvere et al. 2019).

877

878 **In situ hybridization**

879 Mouse embryos homozygous for the *a2KO* mutation and WT littermates were collected at

880 E10.5 and fixed overnight in 4% paraformaldehyde in PBS. Probe generation and hybridization

42

881 performed as previously described (Ariza-McNaughton and Krumlauf 2002). Primers used to

882 generate probes for *Hoxa2* targets from cDNA as follows:

Gene	Forward Primer	Reverse Primer
Prrx1	CGGCACAAGCAGACGAAAG	AGTAGCCATGGCGCTGTACG
Nr2f1	AACGGGGATCCTCTCAATGG	TGAAACTGCTCCCTGACAGC
Tshz1	GTAGAGAAGGTCACGGGCAA	GCCCGTGAACTTGGAGATG

883 Each gene was assayed in 4-10 embryos of each genotype and only those with consistent

884 patterns were considered significant. Z-stack images were acquired with a Leica MZ16

885 steromicroscope and subsequently processed with Helicon Focus 6.8.0 software (Helicon Soft

886 Ltd.) to create a projection of all imagines into a single high-focus photo.

887

888 Skeletal staining

889 Mouse embryos heterozygous or homozygous for the *a2KO* allele along with WT littermates

890 were collected at E18.5, euthanized in PBS on ice for 1 hour, and then fixed and stored in ice

891 cold 100% ethanol. Staining with Alcian Blue and Alizarin Red was performed as previously

892 described (Rigueur and Lyons 2014).

893

894 **Data Availability**

895 The bulk and single-cell RNAseq data generated as part of this manuscript have been deposited

896 into the National Center for Biotechnology Information Gene Expression Omnibus (NCBI GEO)

897 database – accession number GSE164111. Files generated during analysis have been included

898 as Supplementary Tables where deemed appropriate. Original data underlying this manuscript

899 can be accessed from the Stowers Original Data Repository at

900 http://www.stowers.org/research/publications/libpb-1598.

Supplementary Table Legends

Table S1. Summary table of genes differentially expressed in bRNAseq data between WT PA1 and WT PA2 across timepoints.

Table S2. Results of differential expression analysis from bRNAseq data between WT PA1 and WT PA2 at E9.0 including adjusted p-value and log(fold change).

Table S3. Results of differential expression analysis from bRNAseq data between WT PA1 and WT PA2 at E9.5 including adjusted p-value and log(fold change).

Table S4. Results of differential expression analysis from bRNAseq data between WT PA1 and WT PA2 at E10.0 including adjusted p-value and log(fold change).

Table S5. Results of differential expression analysis from bRNAseq data between WT PA1 and WT PA2 at E10.5 including adjusted p-value and log(fold change).

Table S6. Summary table of genes differentially expressed in bRNAseq data between WT PA2 and *a2KO* PA2 across timepoints.

Table S7. Results of differential expression analysis from bRNAseq data between WT PA2 and *a2KO* PA2 at E9.0 including adjusted p-value and log(fold change).

Table S8. Results of differential expression analysis from bRNAseq data between WT PA2 and *a2KO* PA2 at E9.5 including adjusted p-value and log(fold change).

Table S9. Results of differential expression analysis from bRNAseq data between WT PA2 and *a2KO* PA2 at E10.0 including adjusted p-value and log(fold change).

Table S10. Results of differential expression analysis from bRNAseq data between WT PA2 and *a2KO* PA2 at E10.5 including adjusted p-value and log(fold change).

Table S11. Marker genes for all clusters in scRNAseq dataset at E10.5.

Table S12. Genes corresponding to PA1 and PA2 transcriptional signatures based on WT PA1 vs. WT PA2 differential expression analysis.

44

925   Table S13. Putative *Hoxa2*-repressed PA1 specifiers. Genes identified from bRNAseq, as well as

926   scRNAseq clusters 1-4. For each gene, 1 corresponds to being statistically significant in a given

927   dataset, 0 indicates not significant. In the last column, B indicates it is the nearest gene to a

928   HOXA2 binding site from (Donaldson et al. 2012), N indicates that it is not.

929   Table S14. Putative *Hoxa2*-activated PA2 specifiers. Genes identified from bRNAseq, as well as

930   scRNAseq clusters 1-4. For each gene, 1 corresponds to being statistically significant in a given

931   dataset, 0 indicates not significant. In the last column, B indicates it is the nearest gene to a

932   HOXA2 binding site from (Donaldson et al. 2012), N indicates that it is not.

933   Table S15. GO terms for putative *Hoxa2*-repressed PA1 specifiers.

934   Table S16. GO terms for putative *Hoxa2*-activated PA2 specifiers.

935   Table S17. Summary table of genes differentially expressed in bRNAseq data between WT PA1

936   and *a2KO* PA1 across timepoints.

937   Table S18. Results of differential expression analysis from bRNAseq data between WT PA1 and

938   *a2KO* PA1 at E9.0 including adjusted p-value and log(fold change).

939   Table S19. Results of differential expression analysis from bRNAseq data between WT PA1 and

940   *a2KO* PA1 at E9.5 including adjusted p-value and log(fold change).

941   Table S20. Results of differential expression analysis from bRNAseq data between WT PA1 and

942   *a2KO* PA1 at E10.0 including adjusted p-value and log(fold change).

943   Table S21. Results of differential expression analysis from bRNAseq data between WT PA1 and

944   *a2KO* PA1 at E10.5 including adjusted p-value and log(fold change).

945

Acknowledgements

Competing Interests

IP: Supported by Graduate School of the Stowers Institute for Medical Research and NIH F31.

PAT: Employed and research funded by Stowers Institute for Medical Research; Stipend from American Association of Anatomists for being Editor-in-Chief of *Developmental Dynamics*.

46

974   RK: Employed and research funded by Stowers Institute for Medical Research; Member of

975   Scientific Review Board of Howard Hughes Medical Institute; Member of the Board of Directors

976   of the Society for Developmental Biology; Co-inventor listed on patents licensed by the Stowers

977   Institute to Amgen for a drug to regulate bone density.

978

References

Alexander T, Nolte C, Krumlauf R. 2009. Hox genes and segmentation of the hindbrain and axial skeleton. *Annu Rev Cell Dev Biol* **25**: 431-456.

Amin S, Donaldson IJ, Zannino DA, Hensman J, Rattray M, Losa M, Spitz F, Ladam F, Sagerstrom C, Bobola N. 2015. Hoxa2 selectively enhances Meis binding to change a branchial arch ground state. *Dev Cell* **32**: 265-277.

Ariza-McNaughton L, Krumlauf R. 2002. Non-radioactive in situ hybridization: simplified procedures for use in whole-mounts of mouse and chick embryos. *Int Rev Neurobiol* **47**: 239-250.

Barske L, Rataud P, Behizad K, Del Rio L, Cox SG, Crump JG. 2018. Essential Role of Nr2f Nuclear Receptors in Patterning the Vertebrate Upper Jaw. *Dev Cell* **44**: 337-347 e335.

Bobola N, Carapuco M, Ohnemus S, Kanzler B, Leibbrandt A, Neubuser A, Drouin J, Mallo M. 2003. Mesenchymal patterning by Hoxa2 requires blocking Fgf-dependent activation of Ptx1. *Development* **130**: 3403-3414.

Brunskill EW, Potter AS, Distasio A, Dexheimer P, Plassard A, Aronow BJ, Potter SS. 2014. A gene expression atlas of early craniofacial development. *Dev Biol* **391**: 133-146.

Butler A, Hoffman P, Smibert P, Papalexi E, Satija R. 2018. Integrating single-cell transcriptomic data across different conditions, technologies, and species. *Nat Biotechnol* **36**: 411-420.

Cao J, Spielmann M, Qiu X, Huang X, Ibrahim DM, Hill AJ, Zhang F, Mundlos S, Christiansen L, Steemers FJ et al. 2019. The single-cell transcriptional landscape of mammalian organogenesis. *Nature* **566**: 496-502.

Carroll SB. 1995. Homeotic genes and the evolution of arthropods and chordates. *Nature* **376**: 479-485.

Chen Y, Lun AT, Smyth GK. 2016. From reads to genes to pathways: differential expression analysis of RNA-Seq experiments using Rsubread and the edgeR quasi-likelihood pipeline. *F1000Res* **5**: 1438.

Cong L, Ran FA, Cox D, Lin S, Barretto R, Habib N, Hsu PD, Wu X, Jiang W, Marraffini LA et al. 2013. Multiplex genome engineering using CRISPR/Cas systems. *Science* **339**: 819-823.

Coré N, Caubit X, Metchat A, Boned A, Djabali M, Fasano L. 2007. Tshz1 is required for axial skeleton, soft palate and middle ear development in mice. *Dev Biol* **308**: 407-420.

Couly G, Grapin-Botton A, Coltey P, Ruhin B, Le Douarin NM. 1998. Determination of the identity of the derivatives of the cephalic neural crest: incompatibility between *Hox* gene expression and lower jaw development. *Development* **128**: 3445-3459.

Couly GF, Coltey PM, Le Douarin NM. 1993. The triple origin of skull in higher vertebrates- a study in quail-chick chimeras. *Development* **117**: 409-429.

Crane JF, Trainor PA. 2006. Neural crest stem and progenitor cells. *Annu Rev Cell Dev Biol* **22**: 267-286.

Dash S, Trainor PA. 2020. The development, patterning and evolution of neural crest cell differentiation into cartilage and bone. *Bone* **137**: 115409.

De Kumar B, Parker HJ, Parrish ME, Lange JJ, Slaughter BD, Unruh JR, Paulson A, Krumlauf R. 2017. Dynamic regulation of Nanog and stem cell-signaling pathways by Hoxa1 during early neuro-ectodermal differentiation of ES cells. *Proc Natl Acad Sci U S A* **114**: 5838-5845.

Dixon J, Jones NC, Sandell LL, Jayasinghe SM, Crane J, Rey JP, Dixon MJ, Trainor PA. 2006. Tcof1/Treacle is required for neural crest cell formation and proliferation deficiencies that cause craniofacial abnormalities. *Proc Natl Acad Sci U S A* **103**: 13403-13408.

Donaldson IJ, Amin S, Hensman JJ, Kutejova E, Rattray M, Lawrence N, Hayes A, Ward CM, Bobola N. 2012. Genome-wide occupancy links Hoxa2 to Wnt-beta-catenin signaling in mouse embryonic development. *Nucleic Acids Res* **40**: 3990-4001.

1024   Dooley CM, Wali N, Sealy IM, White RJ, Stemple DL, Collins JE, Busch-Nentwich EM. 2019. The gene
1025   regulatory basis of genetic compensation during neural crest induction. *PLoS Genet* **15**:
1026   e1008213.
1027   Etchevers HC, Dupin E, Le Douarin NM. 2019. The diverse neural crest: from embryology to human
1028   pathology. *Development* **146**.
1029   Gammill LS, Bronner-Fraser M. 2002. Genomic analysis of neural crest induction. *Development* **129**:
1030   5731-5741.
1031   Gendron-Maguire M, Mallo M, Zhang M, Gridley T. 1993. Hoxa-2 mutant mice exhibit homeotic
1032   transformation of skeletal elements derived from cranial neural crest. *Cell* **75**: 1317-1331.
1033   Grammatopoulos GA, Bell E, Toole L, Lumsden A, Tucker AS. 2000. Homeotic transformation of branchial
1034   arch identity after Hoxa2 overexpression. *Development* **127**: 5355-5365.
1035   Green SA, Simoes-Costa M, Bronner ME. 2015. Evolution of vertebrates as viewed from the crest. *Nature*
1036   **520**: 474-482.
1037   Hainer SJ, Fazzio TG. 2019. High-Resolution Chromatin Profiling Using CUT&RUN. *Curr Protoc Mol Biol*
1038   **126**: e85.
1039   Hunt P, Gulisano M, Cook M, Sham MH, Faiella A, Wilkinson D, Boncinelli E, Krumlauf R. 1991. A distinct
1040   Hox code for the branchial region of the vertebrate head. *Nature* **353**: 861-864.
1041   Hunter MP, Prince VE. 2002. Zebrafish hox paralogue group 2 genes function redundantly as selector
1042   genes to pattern the second pharyngeal arch. *Dev Biol* **247**: 367-389.
1043   Jones NC, Lynn ML, Gaudenz K, Sakai D, Aoto K, Rey JP, Glynn EF, Ellington L, Du C, Dixon J et al. 2008.
1044   Prevention of the neurocristopathy Treacher Collins syndrome through inhibition of p53
1045   function. *Nat Med* **14**: 125-133.
1046   Kanzler B, Kuschert SJ, Liu Y-H, Mallo M. 1998. *Hoxa2* restricts the chondrogenic domain and inhibits
1047   bone formation during development of the branchial area. *Development* **125**: 2587-2597.
1048   Kim D, Pertea G, Trapnell C, Pimentel H, Kelley R, Salzberg SL. 2013. TopHat2: accurate alignment of
1049   transcriptomes in the presence of insertions, deletions and gene fusions. *Genome Biol* **14**: R36.
1050   Kirilenko P, He G, Mankoo BS, Mallo M, Jones R, Bobola N. 2011. Transient activation of meox1 is an
1051   early component of the gene regulatory network downstream of hoxa2. *Molecular and cellular*
1052   *biology* **31**: 1301-1308.
1053   Kitazawa T, Fujisawa K, Narboux-Neme N, Arima Y, Kawamura Y, Inoue T, Wada Y, Kohro T, Aburatani H,
1054   Kodama T et al. 2015. Distinct effects of Hoxa2 overexpression in cranial neural crest
1055   populations reveal that the mammalian hyomandibular-ceratohyal boundary maps within the
1056   styloid process. *Dev Biol* **402**: 162-174.
1057   Knecht AK, Bronner-Fraser M. 2002. Induction of the neural crest: a multigene process. *Nat Rev Genet* **3**:
1058   453-461.
1059   Kontges G, Lumsden A. 1996. Rhombencephalic neural crest segmentation is preserved throughout
1060   craniofacial ontogeny. *Development* **122**: 3229-3242.
1061   LaBonne C, Bronner-Fraser M. 1998. Induction and patterning of the neural crest, a stem cell-like
1062   precursor population. *J Neurobiol* **36**: 175-189.
1063   LaBonne C, Bronner-Fraser M. 1999. Molecular mechanisms of neural crest formation. *Annu Rev Cell Dev*
1064   *Biol* **15**: 81-112.
1065   Laing AF, Lowell S, Brickman JM. 2015. Gro/TLE enables embryonic stem cell differentiation by
1066   repressing pluripotent gene expression. *Dev Biol* **397**: 56-66.
1067   Le Douarin N, Kalcheim C. 1999. *The Neural Crest*. Cambridge University Press, Cambridge, UK ; New
1068   York, NY, USA.
1069   Lex A, Gehlenborg N, Strobelt H, Vuillemot R, Pfister H. 2014. UpSet: Visualization of Intersecting Sets.
1070   *IEEE Trans Vis Comput Graph* **20**: 1983-1992.

1071 Lumb R, Buckberry S, Secker G, Lawrence D, Schwarz Q. 2017. Transcriptome profiling reveals expression
1072   signatures of cranial neural crest cells arising from different axial levels. *BMC Dev Biol* **17**: 5.
1073 Maconochie M, Krishnamurthy R, Nonchev S, Meier P, Manzanares M, Mitchell PJ, Krumlauf R. 1999.
1074   Regulation of *Hoxa2* in cranial neural crest cells involves members of the *AP-2* family.
1075   *Development* **126**: 1483-1494.
1076 Maconochie MK, Nonchev S, Studer M, Chan SK, Popperl H, Sham MH, Mann RS, Krumlauf R. 1997.
1077   Cross-regulation in the mouse *HoxB* complex: the expression of *Hoxb2* in rhombomere 4 is
1078   regulated by *Hoxb1*. *Genes and Development* **11**: 1885-1896.
1079 Mallo M, Wellik DM, Deschamps J. 2010. Hox genes and regional patterning of the vertebrate body plan.
1080   *Dev Biol* **344**: 7-15.
1081 Martik ML, Bronner ME. 2017. Regulatory Logic Underlying Diversification of the Neural Crest. *Trends in*
1082   *genetics : TIG* **33**: 715-727.
1083 Martik ML, Gandhi S, Uy BR, Gillis JA, Green SA, Simoes-Costa M, Bronner ME. 2019. Evolution of the
1084   new head by gradual acquisition of neural crest regulatory circuits. *Nature* **574**: 675-678.
1085 Martin JF, Bradley A, Olson EN. 1995. The paired-like homeo box gene MHox is required for early events
1086   of skeletogenesis in multiple lineages. *Genes Dev* **9**: 1237-1249.
1087 McEllin JA, Alexander TB, Tumpel S, Wiedemann LM, Krumlauf R. 2016. Analyses of fugu hoxa2 genes
1088   provide evidence for subfunctionalization of neural crest cell and rhombomere cis-regulatory
1089   modules during vertebrate evolution. *Dev Biol* **409**: 530-542.
1090 McGinnis CS, Murrow LM, Gartner ZJ. 2019. DoubletFinder: Doublet Detection in Single-Cell RNA
1091   Sequencing Data Using Artificial Nearest Neighbors. *Cell Syst* **8**: 329-337 e324.
1092 Minoux M, Antonarakis GS, Kmita M, Duboule D, Rijli FM. 2009. Rostral and caudal pharyngeal arches
1093   share a common neural crest ground pattern. *Development* **136**: 637-645.
1094 Minoux M, Holwerda S, Vitobello A, Kitazawa T, Kohler H, Stadler MB, Rijli FM. 2017. Gene bivalency at
1095   Polycomb domains regulates cranial neural crest positional identity. *Science* **355**.
1096 Minoux M, Kratochwil CF, Ducret S, Amin S, Kitazawa T, Kurihara H, Bobola N, Vilain N, Rijli FM. 2013.
1097   Mouse Hoxa2 mutations provide a model for microtia and auricle duplication. *Development* **140**:
1098   4386-4397.
1099 Minoux M, Rijli FM. 2010. Molecular mechanisms of cranial neural crest cell migration and patterning in
1100   craniofacial development. *Development* **137**: 2605-2621.
1101 Northcutt R, Gans C. 1983. The genesis of neural crest and epidermal placodes: a reinterpretation of
1102   vertebrate origns. *Q Rev Biol* **58**: 1-28.
1103 Ohnemus S, Bobola N, Kanzler B, Mallo M. 2001. Different levels of Hoxa2 are required for particular
1104   developmental processes. *Mechanisms of development* **108**: 135-147.
1105 Parker HJ, Bronner ME, Krumlauf R. 2016. The vertebrate Hox gene regulatory network for hindbrain
1106   segmentation: Evolution and diversification: Coupling of a Hox gene regulatory network to
1107   hindbrain segmentation is an ancient trait originating at the base of vertebrates. *BioEssays :*
1108   *news and reviews in molecular, cellular and developmental biology* **38**: 526-538.
1109 Parker HJ, De Kumar B, Green SA, Prummel KD, Hess C, Kaufman CK, Mosimann C, Wiedemann LM,
1110   Bronner ME, Krumlauf R. 2019. A Hox-TALE regulatory circuit for neural crest patterning is
1111   conserved across vertebrates. *Nature communications* **10**: 1189.
1112 Parker HJ, Krumlauf R. 2020. A Hox gene regulatory network for hindbrain segmentation. *Curr Top Dev*
1113   *Biol* **139**: 169-203.
1114 Parker HJ, Pushel I, Krumlauf R. 2018. Coupling the roles of Hox genes to regulatory networks patterning
1115   cranial neural crest. *Dev Biol* **444 Suppl 1**: S67-S78.
1116 Pasqualetti M, Ori M, Nardi I, Rijli FM. 2000. Ectopic Hoxa2 induction after neural crest migration results
1117   in homeosis of jaw elements in Xenopus. *Development* **127**: 5367-5378.

1118　Prakash V, Carson BB, Feenstra JM, Dass RA, Sekyrova P, Hoshino A, Petersen J, Guo Y, Parks MM, Kurylo
1119　　　CM et al. 2019. Ribosome biogenesis during cell cycle arrest fuels EMT in development and
1120　　　disease. *Nat Commun* **10**: 2110.
1121　Rada-Iglesias A, Bajpai R, Prescott S, Brugmann SA, Swigut T, Wysocka J. 2012. Epigenomic annotation of
1122　　　enhancers predicts transcriptional regulators of human neural crest. *Cell Stem Cell* **11**: 633-648.
1123　Raudvere U, Kolberg L, Kuzmin I, Arak T, Adler P, Peterson H, Vilo J. 2019. g:Profiler: a web server for
1124　　　functional enrichment analysis and conversions of gene lists (2019 update). *Nucleic Acids Res* **47**:
1125　　　W191-W198.
1126　Rigueur D, Lyons KM. 2014. Whole-mount skeletal staining. *Methods Mol Biol* **1130**: 113-121.
1127　Rijli FM, Mark M, Lakkaraju S, Dierich A, Dollé P, Chambon P. 1993. A homeotic transformation is
1128　　　generated in the rostral branchial region of the head by disruption of Hoxa-2, which acts as a
1129　　　selector gene. *Cell* **75**: 1333-1349.
1130　Santagati F, Minoux M, Ren SY, Rijli FM. 2005. Temporal requirement of Hoxa2 in cranial neural crest
1131　　　skeletal morphogenesis. *Development* **132**: 4927-4936.
1132　Sauka-Spengler T, Meulemans D, Jones M, Bronner-Fraser M. 2007. Ancient evolutionary origin of the
1133　　　neural crest gene regulatory network. *Developmental cell* **13**: 405-420.
1134　Schilling TF, Prince V, Ingham PW. 2001. Plasticity in zebrafish hox expression in the hindbrain and
1135　　　cranial neural crest. *Dev Biol* **231**: 201-216.
1136　Schmidl C, Rendeiro AF, Sheffield NC, Bock C. 2015. ChIPmentation: fast, robust, low-input ChIP-seq for
1137　　　histones and transcription factors. *Nat Methods* **12**: 963-965.
1138　Simoes-Costa M, Bronner ME. 2015. Establishing neural crest identity: a gene regulatory recipe.
1139　　　*Development* **142**: 242-257.
1140　Soldatov R, Kaucka M, Kastriti ME, Petersen J, Chontorotzea T, Englmaier L, Akkuratova N, Yang Y, Häring
1141　　　M, Dyachuk V et al. 2019. Spatiotemporal structure of cell fate decisions in murine neural crest.
1142　　　*Science* **364**.
1143　Square T, Jandzik D, Romasek M, Cerny R, Medeiros DM. 2017. The origin and diversification of the
1144　　　developmental mechanisms that pattern the vertebrate head skeleton. *Dev Biol* **427**: 219-229.
1145　Stuart T, Butler A, Hoffman P, Hafemeister C, Papalexi E, Mauck WM, 3rd, Hao Y, Stoeckius M, Smibert P,
1146　　　Satija R. 2019. Comprehensive Integration of Single-Cell Data. *Cell* **177**: 1888-1902 e1821.
1147　Tambalo M, Mitter R, Wilkinson DG. 2020. A single cell transcriptome atlas of the developing zebrafish
1148　　　hindbrain. *Development* **147**.
1149　Terrazas K, Dixon J, Trainor PA, Dixon MJ. 2017. Rare syndromes of the head and face: mandibulofacial
1150　　　and acrofacial dysostoses. *Wiley interdisciplinary reviews Developmental biology* **6**.
1151　Trainor P, Krumlauf R. 2000a. Plasticity in mouse neural crest cells reveals a new patterning role for
1152　　　cranial mesoderm. *Nature cell biology* **2**: 96-102.
1153　Trainor PA, Ariza-McNaughton L, Krumlauf R. 2002. Role of the isthmus and FGFs in resolving the
1154　　　paradox of neural crest plasticity and prepatterning. *Science* **295**: 1288-1291.
1155　Trainor PA, Krumlauf R. 2000b. Patterning the cranial neural crest: Hindbrain segmentation and *Hox*
1156　　　gene plasticity. *Nature reviews Neuroscience* **1**: 116-124.
1157　Trainor PA, Krumlauf R. 2001. Hox genes, neural crest cells and branchial arch patterning. *Current*
1158　　　*Opinion in Cell Biology* **13**: 698-705.
1159　Tümpel S, Cambronero F, Ferretti E, Blasi F, Wiedemann LM, Krumlauf R. 2007. Expression of Hoxa2 in
1160　　　rhombomere 4 is regulated by a conserved cross-regulatory mechanism dependent upon Hoxb1.
1161　　　*Dev Biol* **302**: 646-660.
1162　Tümpel S, Cambronero F, Wiedemann LM, Krumlauf R. 2006. Evolution of *cis* elements in the differential
1163　　　expression of two *Hoxa2* coparalogous genes in pufferfish (*Takifugu rubripes*). *Proc Natl Acad Sci*
1164　　　*U S A* **103**: 5419-5424.

1165   Vieux-Rochas M, Mascrez B, Krumlauf R, Duboule D. 2013. Combined function of HoxA and HoxB
1166   clusters in neural crest cells. *Dev Biol* **382**: 293-301.
1167   Watt KEN, Neben CL, Hall S, Merrill AE, Trainor PA. 2018. tp53-dependent and independent signaling
1168   underlies the pathogenesis and possible prevention of Acrofacial Dysostosis-Cincinnati type.
1169   *Hum Mol Genet* **27**: 2628-2643.
1170   Weaver KN, Watt KE, Hufnagel RB, Navajas Acedo J, Linscott LL, Sund KL, Bender PL, Konig R, Lourenco
1171   CM, Hehr U et al. 2015. Acrofacial Dysostosis, Cincinnati Type, a Mandibulofacial Dysostosis
1172   Syndrome with Limb Anomalies, Is Caused by POLR1A Dysfunction. *Am J Hum Genet* **96**: 765-
1173   774.
1174   Xu J, Liu H, Lan Y, Adam M, Clouthier DE, Potter S, Jiang R. 2019. Hedgehog signaling patterns the oral-
1175   aboral axis of the mandibular arch. *Elife* **8**.

1176

1177

1178

1179